Title	Four- and eight-node hybrid-Trefftz quadrilateral finite element models for helmholtz problem
Author(s)	Sze, KY; Liu, GH; Fan, H
Citation	Computer Methods In Applied Mechanics And Engineering, 2010, v. 199 n. 9-12, p. 598-614
Issued Date	2010
URL	http://hdl.handle.net/10722/124827
Rights	Creative Commons: Attribution 3.0 Hong Kong License

Four- and Eight-node Hybrid-Trefftz Quadrilateral Finite Element Models for Helmholtz Problem

K.Y.Sze[1]*, G.H.Liu[1], H.Fan[2]

1 *Department of Mechanical Engineering, The University of Hong Kong, Pokfulam, Hong Kong, P.R.CHINA.*

2 *School of Mechanical & Aerospace Engineering, Nanyang Technological University, Singapore 639798.*

* Correspondence author (email: kysze@hku.hk)

ABSTRACT

In this paper, four- and eight-node quadrilateral finite element models which can readily be incorporated into the standard finite element program framework are devised for plane Helmholtz problems. In these models, frame (boundary) and domain approximations are defined. The former is obtained by nodal interpolation and the latter is truncated from Trefftz solution sets. The equality of the two approximations are enforced along the element boundary. Both the Bessel and plane wave solutions are employed to construct the domain approximation. For full rankness, a minimal of four and eight domain modes are required for the four- and eight-node elements, respectively. By using local coordinates and directions, rank sufficient and invariant elements with minimal and close to minimal numbers of domain approximation modes are devised. In most tests, the proposed hybrid-Trefftz elements with the same number of nodes yield close solutions. In absolute majority of the tests, the proposed elements are considerably more accurate than their single-field counterparts.

Keywords: hybrid-Trefftz, quadrilateral, finite element, Helmholtz, Bessel, plane wave.

Appeared in *Computer Methods in Applied Mechanics & Engineering* 199: 598-614 (2010)

1. INTRODUCTION

In the hybrid finite element method for stress/structural analyses, the displacement-based finite element models are enhanced by introducing stress, strain or another displacement as the additional field variable(s) to the displacement obtained by nodal interpolation [1-10]. In the case of the hybrid-displacement method, the additional field is a domain displacement which leads to equilibrating stress and may also satisfy some homogeneous boundary conditions [2,3,10]. This category of hybrid elements are also known as hybrid-Trefftz or Trefftz elements linked by the displacement-frame or the boundary displacement [4,6-10]. The underlying reason is that the domain displacement is truncated from a Trefftz solution set which is the basis of the Trefftz non-singular boundary element methods.

A major challenge in finite element analyses of Helmholtz problems is that the solutions are spatially oscillating in the entire problem domains. This contrasts sharply with stress analyses in which high displacement gradients only occur in the stress concentration regions. While considerable computational saving can be realized by using graded meshes in stress analyses, the practice is not applicable to Helmholtz problems. Hence, the mesh requirement induces tremendous computing load when the wavenumber increases. To better tackle the issue, a number of wave-based approaches that make use of solution sets for the wave or Helmholtz equations have been proposed in the last decades. These include the Trefftz methods [11-18], the plane wave basis method [19-22] and the discontinuous enrichment method [23,24], among others.

Though a number of Trefftz boundary element methods have been formulated for Helmholtz problems [11-15], Trefftz finite element models do not appear to be abundant. Among them, the least-square models [16,17] and the traction-frame models [18] can be noted. All Trefftz models possess their own domain approximations which are extracted from Trefftz solution sets. The least-square models are formulated by minimizing a weighted sum of the error norms of the boundary conditions and inter-element continuity conditions on the domain approximations of adjacent elements. The traction-frame models are equipped with boundary “traction” approximations and domain approximations can be condensed at the element level.

In the plane wave basis method, the plane wave solutions are employed as the nodal enrichment functions in the context of the partition of unity finite element method [19-22]. The value of the Helmholtz variable at a node is the sum of plane wave solutions which represent plane waves propagating along different directions. Within the element, the Helmholtz variable is obtained by the conventional nodal interpolation. Thus, the system equation unknowns are the amplitudes of the plane waves at the nodes but not the nodal value of the Helmholtz variable.

In the multiscale-based discontinuous enrichment method, the coarse scale approximation constructed by the conventional nodal interpolation is enriched by plane wave solutions. The enrichment which is intended to resolve the fine scale phenomenon induces discontinuity across the inter-element boundary [23,24]. Weak enforcement of the continuity is implemented through Lagrange multipliers. While the fine scale enrichments can be condensed at element level, the multipliers which link the enrichments of adjacent elements enter the global equation.

In this paper, hybrid-Trefftz four-node and eight-node quadrilateral elements will be formulated. Unlike the previous Trefftz finite element models, the present elements can readily be incorporated into the standard finite element program framework. In these models, independent frame (boundary) and domain approximations of the Helmholtz variable are defined. The frame approximation is obtained by nodal interpolation and the domain approximation is truncated from Trefftz solution sets of the Helmholtz equation. Along the edges of the four-node and eight-node elements, the frame variables are obtained by linear and quadratic nodal interpolations, respectively. Equality of the two approximations are enforced along the element boundary. The hybrid variational functional employed in the formulation is analogous to the functional used in elasticity hybrid-Trefftz elements with displacement-frame approximations [2,3,4,8,10,18]. The functional enforces the Helmholtz equation on the frame approximation, the natural boundary and an inter-element continuity conditions on the domain approximation as well as the equality of the domain and boundary approximations [25]. Both the Bessel and plane wave solutions are employed to construct the domain approximation. For the full rankness, a minimal of four and eight domain approximation modes are required for the four- and eight-node elements, respectively. By using local coordinates, rank sufficient and invariant elements [26,27] with the minimal and close to minimal numbers of domain approximation modes are devised. Numerical tests show that all the hybrid-Trefftz elements are more accurate than their single-field counterparts.

2. THE CONVENTIONAL FINITE ELEMNET FORMULATION

Helmholtz equation is often introduced by using the steady state acoustics. The Helmholtz variable u can be the spatial amplitude of the pressure or the velocity potential. This paper will restrict itself to bounded domain problems. With the problem domain Ω partitioned into sub-domains or finite elements Ω^es and ∇ denoting $(\partial/\partial x, \partial/\partial y)^T$, the problem can be summarized as:

(a) Helmholtz equation: $\nabla^2 u + k^2 u = 0$ in all Ω^e

(b) the natural boundary condition: $\mathbf{n}^T \nabla u = \bar{t}$ on all Γ_t^e

(c) the essential boundary condition: $u = \bar{u}$ and $\delta u = 0$ on all Γ_u^e

(d) the reciprocity condition: $(\mathbf{n}^T \nabla u)^+ + (\mathbf{n}^T \nabla u)^- = 0$ on all Γ_m^e

(e) the compatibility condition: $u^+ = u^-$ and $\delta u^+ = \delta u^-$ on all Γ_m^e

In the above expressions, $\nabla^2 = \nabla^T \nabla$ is the Laplace operator, **n** is the outward unit normal vector to the element boundary, k is the wave number, δ is the variational symbol and Γ_m^e is the inter-element boundary. Moreover, $()^+$ and $()^-$ denote the braced quantities at the two sides of Γ_m^e. In the absence of dissipation, k is real. Otherwise, it is complex. For simplicity, it will be assumed as usual that element boundary or frame $\partial\Omega^e$ can be partitioned into the non-overlapping portions Γ_t^e, Γ_u^e and Γ_m^e, i.e.

$$\Gamma_t^e \cup \Gamma_u^e \cup \Gamma_m^e = \partial\Omega^e \quad \text{and} \quad \Gamma_t^e \cap \Gamma_u^e = \Gamma_u^e \cap \Gamma_m^e = \Gamma_m^e \cap \Gamma_t^e = \text{null}. \tag{1}$$

The elemental variational functional for the conventional finite element formulation of the Helmholtz problem is well-known to be:

$$\Pi^e = \frac{1}{2} \int_{\Omega^e} \left((\nabla u)^T \nabla u - k^2 u^2 \right) d\Omega - \int_{\Gamma_t^e} \bar{t} u \, d\Gamma \tag{2}$$

in which u is obtained from the conventional nodal interpolation. The functional for the problem domain is equal to the sum of all Π^es. By invoking (1) and the divergence theorem:

$$\int_{\Omega^e} \left((\nabla f)^T \nabla h + h \nabla^2 f \right) d\Omega = \int_{\partial\Omega^e} h (\mathbf{n}^T \nabla f) \, d\Gamma \tag{3}$$

for any smooth functions f and h in Ω^e, variation of (2) can be written as:

$$\delta\Pi^e = -\int_{\Omega^e} (\nabla^2 u + k^2 u) \delta u \, d\Omega + \int_{\Gamma_t^e} (\mathbf{n}^T \nabla u - \bar{t}) \delta u \, d\Gamma + \int_{\Gamma_m^e} (\mathbf{n}^T \nabla u) \delta u \, d\Gamma \tag{4}$$

The first and second integrals enforce (a) and (b). The last integral when co-considered with those from the neighborhood elements enforces (d). Conditions (c) and (e) can be easily satisfied by the interpolated u and are taken as prerequisites .

Figure 1a shows an eight-node quadrilateral element in the global (x,y) coordinate plane. In four-node elements, there are only four corner nodes and the element edges must be straight. The global coordinates and the field variable u can be interpolated and expressed as:

$$\begin{Bmatrix} x \\ y \end{Bmatrix} = \sum_{i=1}^{n} N_i \begin{Bmatrix} x_i \\ y_i \end{Bmatrix} \quad \text{and} \quad u = \sum_{i=1}^{n} N_i u_i = [N_1, ..., N_n] \begin{Bmatrix} u_1 \\ \vdots \\ u_n \end{Bmatrix} = \mathbf{Nd} \tag{5}$$

where n is the number of nodes in the element. The nodal interpolation functions N_is are functions of the natural coordinates ξ and $\eta \in$[-1,+1]. They can be found in standard finite element textbooks and will not be repeated here. The interpolation matrix **N** and the vector of nodal dofs **d** are self-defined. With (5) substituted into (2),

$$\Pi^e = \frac{1}{2}\mathbf{d}^T\mathbf{K}_c\mathbf{d} - \mathbf{f}^T\mathbf{d} \tag{6}$$

in which

$$\mathbf{K}_c = \int_{\Omega^e} \left((\nabla\mathbf{N})^T(\nabla\mathbf{N}) - k^2\mathbf{N}^T\mathbf{N} \right) d\Omega = \int_{-1}^{+1}\int_{-1}^{+1} \left((\nabla\mathbf{N})^T(\nabla\mathbf{N}) - k^2\mathbf{N}^T\mathbf{N} \right) J d\xi d\eta \quad \text{and} \quad \mathbf{f} = \int_{\Gamma_t^e} \mathbf{N}^T\bar{t}\, d\Gamma .$$

In the element matrix $\mathbf{K}_c$, $J = (\partial x/\partial\xi)(\partial y/\partial\eta) - (\partial y/\partial\xi)(\partial x/\partial\eta)$ is the Jacobian determinant of the coordinate transformation between (x,y) and (ξ,η).

3. THE HYBRID-TREFFTZ FINITE ELEMNET FORMULATION

The following elemental hybrid functional can be formed by introducing a second Helmholtz approximation g to (2):

$$\Pi_h^e = \frac{1}{2}\int_{\Omega^e} \left((\nabla g)^T\nabla g - k^2 g^2 \right) d\Omega + \int_{\partial\Omega^e} (\mathbf{n}^T\nabla g)(u-g)\, d\Gamma - \int_{\Gamma_t^e} \bar{t}u d\Gamma . \tag{7}$$

In the functional, u, which needs to be known along the frame only, and g can be regarded as the frame and domain variables, respectively. Obviously, (7) degenerates into (2) when u equals g. Again, the functional for the problem domain equals to the sum of all Π_h^es. Variation of Π_h^e is:

$$\delta\Pi_h^e = \int_{\Omega^e} \left((\nabla g)^T\nabla\delta g - k^2 g\delta g \right) d\Omega + \int_{\partial\Omega^e} \left((\mathbf{n}^T\nabla\delta g)(u-g) + (\mathbf{n}^T\nabla g)(\delta u - \delta g) \right) d\Gamma - \int_{\Gamma_t^e} \bar{t}\,\delta u d\Gamma . \tag{8}$$

By invoking the divergence theorem in (3) and assuming that u satisfies (c) and (e) as prerequisites,

$$\delta\Pi_h^e = -\int_{\Omega^e} \left((\nabla^2 g + k^2 g)\delta g \right) d\Omega + \int_{\partial\Omega^e} (\mathbf{n}^T\nabla\delta g)(u-g)\, d\Gamma + \int_{\Gamma_t^e} (\mathbf{n}^T\nabla g - \bar{t})\delta u d\Gamma + \int_{\Gamma_m^e} (\mathbf{n}^T\nabla g)\delta u d\Gamma . \tag{9}$$

It can be seen that the second integral enforces the equality of u and g along the frame $\partial\Omega^e$. The first, third and fourth integrals enforce respectively (a), (b) and (d) with u replaced by g. If g satisfies the

Helmholtz equation, i.e.

$$\nabla^2 g + k^2 g = 0 \tag{10}$$

pointwisely, (7) can be expressed as:

$$\Pi_h^e = \int_{\partial\Omega^e} \left(-\frac{1}{2}(\mathbf{n}^T \nabla g) g + (\mathbf{n}^T \nabla g) u \right) d\Gamma - \int_{\Gamma_t^e} \bar{t} u d\Gamma \tag{11}$$

which only involves boundary integrals and the standard interpolation for u in (5) is still applicable.

Let the domain variable be expressed as:

$$g = \mathbf{P}\boldsymbol{\beta} \tag{12}$$

where $\mathbf{P}$ is the shape function matrix and $\boldsymbol{\beta}$ is the vector of coefficients. With (5) and (12) substituted into (11),

$$\Pi_h^e = -\frac{1}{2}\boldsymbol{\beta}^T \mathbf{H}\boldsymbol{\beta} + \boldsymbol{\beta}^T \mathbf{G}\mathbf{d} - \mathbf{f}^T \mathbf{d} \,. \tag{13}$$

in which

$$\mathbf{H} = \int_{\partial\Omega^e} (\mathbf{n}^T \nabla \mathbf{P})^T \mathbf{P} \, d\Gamma \;\; , \;\; \mathbf{G} = \int_{\partial\Omega^e} (\mathbf{n}^T \nabla \mathbf{P})^T \mathbf{N} \, d\Gamma$$

and $\mathbf{f}$ has been defined in (6). To conduct the boundary integration, four natural coordinates $\xi_i \in [-1,+1]$ are established along the four element edges as shown in Figure 1a and it is trivial that $\xi_1 = \xi$, $\xi_2 = \eta$, $\xi_3 = -\xi$ and $\xi_4 = -\eta$. For the four-node element, the frame variable and the Cartesian coordinates along all its edges are linear and are given as:

$$u = M_i u_i + M_j u_j \;\; , \;\; x = M_i x_i + M_j x_j \;\; , \;\; y = M_i y_i + M_j y_j \tag{14}$$

where $M_i = (1-\xi_i)/2$, $M_j = (1-\xi_j)/2$, $j = \mathrm{mod}(i,4) + 1$ and $\mathrm{mod}(i,4)$ returns the remainder of the integer division $i/4$. Similarly, the expressions are quadratic for the eight-node element and they are:

$$u = M_i u_i + M_m u_m + M_j u_j \;\; , \;\; x = M_i x_i + M_m x_m + M_j x_j \;\; , \;\; y = M_i y_i + M_m y_m + M_j y_j \tag{15}$$

where $M_i = \xi_i(1-\xi_i)/2$, $M_m = 1-\xi_i^2$, $M_j = \xi_i(1+\xi_i)/2$, $j = \mathrm{mod}(i,4) + 1$ and $m = i + 4$. With (14) and (15) , the differential boundary length can be expressed as:

$$d\Gamma = d\xi_i \sqrt{(\partial x/\partial \xi_i)^2 + (\partial y/\partial \xi_i)^2} \;\; , \;\; \mathbf{n} = \frac{1}{\sqrt{(\partial x/\partial \xi_i)^2 + (\partial y/\partial \xi_i)^2}} \begin{Bmatrix} \partial y/\partial \xi_i \\ -\partial x/\partial \xi_i \end{Bmatrix} \tag{16}$$

Hence, the H-matrix and G-matrix can be evaluated as:

$$\mathbf{H} = \sum_{i=1}^{4} \int_{-1}^{+1} \left(\frac{\partial y}{\partial \xi_i}\frac{\partial \mathbf{P}}{\partial x} - \frac{\partial x}{\partial \xi_i}\frac{\partial \mathbf{P}}{\partial y}\right)^T \mathbf{P} d\xi_i \quad \text{and} \quad \mathbf{G} = \sum_{i=1}^{4} \int_{-1}^{+1} \left(\frac{\partial y}{\partial \xi_i}\frac{\partial \mathbf{P}}{\partial x} - \frac{\partial x}{\partial \xi_i}\frac{\partial \mathbf{P}}{\partial y}\right)^T \mathbf{N} d\xi_i \,. \tag{17}$$

in which the N-matrix along each element edge can be constructed from (14) or (15). Furthermore, the H-matrix should be symmetric but it may lose its symmetry if it is numerically evaluated. In our implementation, **H** is symmetrized by averaging itself and its transpose. The variation of (13) with respect to $\boldsymbol{\beta}$ yields:

$$\mathbf{H}\boldsymbol{\beta} = \mathbf{G}\mathbf{d} \quad \text{or} \quad \boldsymbol{\beta} = \mathbf{H}^{-1}\mathbf{G}\mathbf{d} \tag{18}$$

with which the domain variable can be retrieved via (12) as:

$$g = \mathbf{P}\boldsymbol{\beta} = \mathbf{P}\mathbf{H}^{-1}\mathbf{G}\mathbf{d} \tag{19}$$

and $\boldsymbol{\beta}$ can be condensed from Π_h^e. The latter becomes:

$$\Pi_h^e = \frac{1}{2}\mathbf{d}^T(\mathbf{G}^T\mathbf{H}^{-1}\mathbf{G})\mathbf{d} - \mathbf{f}^T\mathbf{d} = \frac{1}{2}\mathbf{d}^T\mathbf{K}_h\mathbf{d} - \mathbf{f}^T\mathbf{d} \tag{20}$$

where $\mathbf{K}_h$ is self-defined and is the element matrix of the hybrid-Trefftz finite element model. Same as the conventional element matrix $\mathbf{K}_c$, $\mathbf{K}_h$ can also be incorporated into the standard finite element program framework.

In designing hybrid elements for stress/structural analyses [1,4,26-30], the two common guidelines on the selection of the stress (domain) modes are that the element should be rank sufficient and invariant. An element is invariant if the element prediction remains intact when (i) the element is translated, (ii) the element is rotated and (iii) the element connectivity, which defines the directions of the parametric coordinates, is changed [26-27]. Accordingly, the invariance requirement can be subdivided into (i) translational invariance, (ii) rotational invariance and (iii) connectivity invariance. Furthermore, the optimal number of stress modes in the hybrid stress element is often considered to be the minimal number that can secure the rank sufficiency.

4. DOMAIN APPROXIMATION FROM BESSEL SOLUTION SET

While the above section outlines the principle to formulate the hybrid-Trefftz element model for the plane Helmholtz problem, it does not discuss the selection of the domain approximation modes. In this and next sections, elements with their domain approximation modes devised from the Bessel and plane wave solution sets will be devised, respectively. The Bessel solution set can be expressed as:

$$\{ J_m(kr)\exp(im\theta),\ m = 0,1,2,\ldots\} \tag{21}$$

where J_m is the m-th order Bessel function of the first kind, $r^2 = x^2 + y^2$, $i^2 = -1$ and $\theta \in [-\pi , \pi]$ is the principal angle of $\tan^{-1}(y/x)$. Both the real and imaginary parts of the members in the solution set can be taken to be domain approximation modes. The elements are not intended to tackle singularity of the field variables within the element domains or on the element boundaries. Hence, the solution set set based upon the Bessel function of the second kind is not considered. To insensitize the Bessel mode to element translation, the following local Cartesian coordinates ($\tilde{x}$, $\tilde{y}$) and polar coordinates ($\tilde{r}$, $\tilde{\theta}$) synchronized with the parametric origin $(x,y)|_{\xi=\eta=0} = (x_o,y_o)$ of the element are defined:

$$\tilde{x} = x - x_o, \quad \tilde{y} = y - y_o, \quad \tilde{r} = \sqrt{\tilde{x}^2 + \tilde{y}^2}, \quad \tilde{\theta} = \tan^{-1}(\tilde{y}/\tilde{x}) \tag{22}$$

as shown in Figure 1a. With them, the following Bessel solution set:

$$\left\{ J_m(k\tilde{r})\exp(im\tilde{\theta}),\ m = 0,1,2,... \right\} \tag{23}$$

is translational invariant. When the element is rotated by any angle α, the real and imaginary modes from J_m can be expanded as:

$$\begin{aligned} &\mathrm{Re}\left(J_m(kr)\exp[im(\theta+\alpha)] \right) = \mathrm{Re}[J_m(kr)\exp(im\theta)]\cos m\alpha - \mathrm{Im}[J_m(kr)\exp(im\theta)]\sin m\alpha\,, \\ &\mathrm{Im}\left(J_m(kr)\exp[im(\theta+\alpha)] \right) = \mathrm{Im}[J_m(kr)\exp(im\theta)]\cos m\alpha - \mathrm{Re}[J_m(kr)\exp(im\theta)]\sin m\alpha \end{aligned} \tag{24}$$

which, therefore, constitute a rotational invariant basis. It is also trivial that $\{ J_m(k\tilde{r})\exp(im\tilde{\theta}) \}$ is insensitive to the chosen connectivity. Hence,

$$\{J_m(k\tilde{r})\exp(im\tilde{\theta})\} = \{\mathrm{Re}(J_m(k\tilde{r})\exp(im\tilde{\theta})), \mathrm{Im}(J_m(k\tilde{r})\exp(im\tilde{\theta}))\} \quad \text{where m = 0, 1, 2, …} \tag{25}$$

is an invariant basis which possess translational, rotational and connectivity invariance. It should be remarked that the sets in (21) and (23) contain infinite members arising from all positive integer m whilst the set in (25) contains only the member(s) of a specific m.

4.1 Four-Node Quadrilateral Elements J5 and J4

A four-node hybrid-Trefftz element has been devised by using the following five-mode shape function matrix [25]:

$$\mathbf{P} = [J_0(k\tilde{r}), J_1(k\tilde{r})\cos\tilde{\theta}, J_1(k\tilde{r})\sin\tilde{\theta}, J_2(k\tilde{r})\cos 2\tilde{\theta}, J_2(k\tilde{r})\sin 2\tilde{\theta}]. \tag{26}$$

The element will here be termed as J5. It is rank sufficient, complete to the second order Bessel functions of the first kind and invariant but the number of domain modes exceeds the minimum or four by one.

To reduce the domain modes to minimal, we first consider a square element with its natural coordinates (ξ,η) and Cartesian coordinate axes (x,y) parallel. By means of a symbolic computational software such as Mathematica, Maple or Maxima, it can be easily proven that the fourth mode in (26) does not couple with any other modes in the H-matrix and the fourth row of the G-matrix (see (13)) is zero regardless of the element size and the k value. In other word, the square J5 element would be identical to the element formulated with the following shape function matrix:

$$\mathbf{P} = [J_0(k\tilde{r}), J_1(k\tilde{r})\cos\tilde{\theta}, J_1(k\tilde{r})\sin\tilde{\theta}, J_2(k\tilde{r})\sin 2\tilde{\theta}] \tag{27}$$

Keeping the natural coordinates parallel to the Cartesian coordinates, we next consider a rectangular J5 element, the coupling terms between the first and fourth modes in the H-matrix and the fourth row in the G-matrix are no longer zero. However, the fourth mode, i.e. $J_2(k\tilde{r})\cos 2\tilde{\theta}$, would only be motivated slightly with respect to the fifth mode, i.e. $J_2(k\tilde{r})\sin 2\tilde{\theta}$, in (26). As an illustration, we consider two J5 rectangular elements with dimensions $1/k\times 1/(5k)$ and $1/(5k)\times 1/k$ which are chosen because more extreme aspect ratios are not encouraged in practical finite element analysis [28]. In both elements, the entries in the fourth and fifth row of $\mathbf{H}^{-1}\mathbf{G}$ are ±0.447 and ±20.2, respectively. As $g = \mathbf{P\beta} = \mathbf{PH}^{-1}\mathbf{Gd}$, see (18), it can be seen that the fifth mode is more dominating than the fourth and, thus, the effect of sacrificing the completeness in J_2 by discarding $J_2(k\tilde{r})\cos 2\tilde{\theta}$ should be small. This point can be seen in the numerical examples.

For general quadrilaterals in which the natural and Cartesian coordinates need not be parallel, the four-mode shape function matrix is taken to be:

$$\mathbf{P} = [J_0(k\tilde{r}), J_1(k\tilde{r})\cos\tilde{\theta}, J_1(k\tilde{r})\sin\tilde{\theta}, J_2(k\tilde{r})\sin 2(\tilde{\theta} - \theta_1)] \tag{28}$$

With the directions of the ξ- and η-axes written as respectively θ_ξ and θ_η as shown in Figure 1b, θ_1 in the above equation is defined to be:

$$\theta_1 = \frac{1}{2}(\theta_\xi + \theta_\eta) - \frac{\pi}{4} \tag{29}$$

The direction was also used by Cook in formulated invariant selectively reduced integrated element [29]. Since a local direction is employed to define the J_2-mode $J_2(k\tilde{r})\sin 2(\tilde{\theta} - \theta_1)$, the mode is rotational invariant. The mode is also connectivity invariant. To illustrate this point, Figure 1c considers the same element but the natural coordinates are now ξ' and η'. It can be noted that

$$\theta_{\xi'} = \theta_\eta, \quad \theta_{\eta'} = \theta_\xi + \pi \quad \text{and} \quad \theta_{1'} = \frac{1}{2}(\theta_{\xi'} + \theta_{\eta'}) - \frac{\pi}{4} = \frac{1}{2}(\theta_\eta + \theta_\xi + \pi) - \frac{\pi}{4} = \theta_1 + \frac{\pi}{2}$$

Under the new connectivity, the J_2-mode is:

$$J_2(k\tilde{r})\sin 2(\tilde{\theta}-\theta_{1'}) = J_2(k\tilde{r})\sin[2(\tilde{\theta}-\theta_1)-\pi] = -J_2(k\tilde{r})\sin 2(\tilde{\theta}-\theta_1)$$

The above mode differs from the J_2-mode in (28) by a negative sign which can be absorbed by the coefficient associated with the mode. One can examine the other two possible connectivity arrangements and confirm that the J_2-mode and, thus, the resultant element are connectivity invariant. It should be remarked that the connectivity invariance cannot be yielded by all locally defined directions such as θ_ξ and θ_η. The resulting invariant element will be termed J4. By chain rule, the derivatives of a general term in **P** can be computed as:

$$\begin{Bmatrix} \partial/\partial x \\ \partial/\partial y \end{Bmatrix}\left(J_m(k\tilde{r})\exp[im(\tilde{\theta}-\phi)]\right) = [\frac{k}{2\tilde{r}}\left(J_{m-1}(k\tilde{r}) - J_{m+1}(k\tilde{r})\right)\begin{Bmatrix} \tilde{x} \\ \tilde{y} \end{Bmatrix} + i\frac{m}{\tilde{r}^2}J_m(k\tilde{r})\begin{Bmatrix} -\tilde{y} \\ \tilde{x} \end{Bmatrix}]\exp[im(\tilde{\theta}-\phi)] \tag{30}$$

where ϕ denotes a constant angle.

4.2 Eight-Node Quadrilateral Elements J9 and J8

Compared with four-node elements, eight-node elements are sometimes preferred as they possess higher convergent rate and can more accurately model curved domain boundaries. Starting from the lowest order terms in (23), the following nine domain modes form an invariant basis:

$$\mathbf{P} = [J_0(k\tilde{r}), J_1(k\tilde{r})\cos\tilde{\theta}, J_1(k\tilde{r})\sin\tilde{\theta}, J_2(k\tilde{r})\cos 2\tilde{\theta}, J_2(k\tilde{r})\sin 2\tilde{\theta},$$

$$J_3(k\tilde{r})\cos 3\tilde{\theta}, J_3(k\tilde{r})\sin 3\tilde{\theta}, J_4(k\tilde{r})\cos 4\tilde{\theta}, J_4(k\tilde{r})\sin 4\tilde{\theta}]. \tag{31}$$

The resulting element is complete to the fourth order Bessel functions, rank sufficient and will be termed as J9.

To derive a rank sufficient element with the minimum number of domain modes, the square element with its natural coordinates (ξ,η) and Cartesian coordinate axes (x,y) parallel is again considered. By means of a symbolic computational software such as Maple, it can be easily proven that the ninth mode does not couple with any other modes in the H-matrix and the ninth row of the G-matrix (see (13) for the definitions of the two matrices) is zero regardless of the element size. In other word, the square J9 element would be identical to the element formulated with the following domain mode shape function matrix:

$$\mathbf{P} = [J_0(k\tilde{r}), J_1(k\tilde{r})\cos\tilde{\theta}, J_1(k\tilde{r})\sin\tilde{\theta}, J_2(k\tilde{r})\cos 2\tilde{\theta}, J_2(k\tilde{r})\sin 2\tilde{\theta},$$

$$J_3(k\tilde{r})\cos 3\tilde{\theta}, J_3(k\tilde{r})\sin 3\tilde{\theta}, J_4(k\tilde{r})\cos 4\tilde{\theta}] \tag{32}$$

Keeping the natural coordinates parallel to the Cartesian coordinates, we then consider a rectangular J9 element, the coupling terms between the fifth and ninth modes in the H-matrix and the ninth row in the G-matrix are no longer zero. However, the ninth mode, i.e. $J_4(k\tilde{r})\sin 4\tilde{\theta}$, would only be motivated slightly with respect to the fifth mode. As an example, two rectangular elements with dimensions $1/k\times 1/(5k)$ and $1/(5k)\times 1/k$ are considered. In both elements, the absolute values of the entries in the eighth rows of $\mathbf{H}^{-1}\mathbf{G}$ range from 5.46 to 249 whilst those in the ninth rows range from 0 to 9.59. The average absolution values of the eighth and ninth rows are 126 and 4.78. As $g = \mathbf{P\beta} = \mathbf{PH}^{-1}\mathbf{Gd}$, see (18), it can be seen that the eighth mode is more dominating than the ninth and, thus, the effect of sacrificing the completeness in J_4 by discarding $J_4(k\tilde{r})\sin 4\tilde{\theta}$ should be small. This point can be seen in the numerical examples.

For general quadrilaterals in which the natural and Cartesian coordinates need not be parallel, the eight-mode shape function matrix is taken to be:

$$\mathbf{P} = [J_0(k\tilde{r}), J_1(k\tilde{r})\cos\tilde{\theta}, J_1(k\tilde{r})\sin\tilde{\theta}, J_2(k\tilde{r})\cos 2\tilde{\theta}, J_2(k\tilde{r})\sin 2\tilde{\theta},$$

$$J_3(k\tilde{r})\cos 3\tilde{\theta}, J_3(k\tilde{r})\sin 3\tilde{\theta}, J_4(k\tilde{r})\cos 4(\tilde{\theta}-\theta_1)] \qquad (33)$$

in which θ_1 has been defined in (29) for the four-node J4 element. By repeating the same arguments of the last section, it can be proven that the J_4 mode $J_4(k\tilde{r})\cos 4(\tilde{\theta}-\theta_1)$ and, thus, the resultant eight-node element are invariant. The element will be termed as J8.

5. DOMAIN APPROXIMATION FROM PLANE WAVE SOLUTION SET

In this section, elements with their domain approximation modes devised from the plane wave solution set will be devised. The solution set can be expressed as:

$$\{p(\varphi_l), l = 1,2,3,...\} = \{\exp[ikr\cos(\theta-\varphi_l)], l = 1,2,3,...\}$$

$$= \{\exp[i(kx\cos\varphi_l + ky\sin\varphi_l)], l = 1,2,3,...\} \qquad (34)$$

where p's are self-defined and φ_l denotes the propagation direction of the plane wave with respect to the global coordinates. The set of angles φ_1, φ_2, … is often picked at equal interval [17-23]. Furthermore,

$$\mathrm{Re}(\,p(\varphi_l \pm \pi)\,) = \cos(kx\cos\varphi_l + ky\sin\varphi_l) = \mathrm{Re}(\,p(\varphi_l)\,),$$

$$\mathrm{Im}(\,p(\varphi_l \pm \pi)\,) = -\sin(kx\cos\varphi_l + ky\sin\varphi_l) = -\mathrm{Im}(\,p(\varphi_l)\,). \qquad (35)$$

In other words, once a direction is included, its reverse should not be employed so as to avoid linearly dependence. It is trivial that when r in (34) is replaced by $\tilde{r}$ defined in (22) and φ_l is a local direction, the following is a translational and rotational invariant basis of the domain modes:

$$\{\tilde{p}(\varphi_l)\} = \{\exp[i(k\tilde{x}\cos\varphi_l + k\tilde{y}\sin\varphi_l)]\} = \{\cos(k\tilde{x}\cos\varphi_l + k\tilde{y}\sin\varphi_l), \sin(k\tilde{x}\cos\varphi_l + k\tilde{y}\sin\varphi_l)\} \quad (36)$$

in which $(\tilde{x}, \tilde{y})$ have been defined in (22).

5.1 Four-Node Quadrilateral Element P4

Let us again consider a square element with its natural coordinates parallel to the Cartesian coordinates. If the wave propagation directions are to be symmetric with respect to the element geometry, the only directions are either parallel to the element edges (i.e. $\{\tilde{p}(0), \tilde{p}(\pi/2)\}$ or the element diagonals $\{\tilde{p}(+\pi/4), \tilde{p}(-\pi/4)\}$. However, the former choice leads to a rank deficient element and should not be adopted. To generalize the latter choice to general quadrilateral elements, θ_1 defined in (29) and Figure 1(b) may be resorted to. The modified domain approximation basis is:

$$\{\tilde{p}(\theta_1 - \frac{\pi}{4}), \tilde{p}(\theta_1 + \frac{\pi}{4})\} \quad (37)$$

which can be easily shown to be connectivity invariant and, thus, invariant.

Next, the trapezoidal element in Figure 2a is considered. In the figure, "—— - ——" is the wave crest $\tilde{x} + \tilde{y} = 0$ in the following mode among (37):

$$\mathrm{Re}(\tilde{p}(\theta_1 + \frac{\pi}{4})) = \mathrm{Re}(\tilde{p}(\frac{\pi}{4})) = \cos\frac{k(\tilde{x} + \tilde{y})}{\sqrt{2}} \quad (38)$$

Clearly, the mode assumes its maximum value along the element boundary away from the nodes. In the four-node frame approximation, the extremum values can only occur at the nodes. To unify the extremum points of the frame and domain approximations along the element boundary, the two element diagonals can be taken to wave crests. This can be achieved by taken the following basis:

$$\{\bar{p}(\theta_2 + \frac{\pi}{2}), \bar{p}(\theta_3 - \frac{\pi}{2})\} = \{\mathrm{Re}(\bar{p}(\theta_2 + \frac{\pi}{2})), \mathrm{Im}(\bar{p}(\theta_2 + \frac{\pi}{2})), \mathrm{Re}(\bar{p}(\theta_3 - \frac{\pi}{2})), \mathrm{Im}(\bar{p}(\theta_3 - \frac{\pi}{2}))\} \quad (39)$$

where

$$\bar{p}(\phi) = \{\exp[i(k\bar{x}\cos\phi + k\bar{y}\sin\phi)]\}, \ \bar{x} = x - x_c, \ \bar{y} = y - y_c.$$

In the above expressions, θ_2 and θ_3 are the directions of the element diagonals whilst (x_c, y_c) is their intersection point as shown in Figure 2(b). The four-node element that employs the four plane wave

domain modes in (39) will be termed as P4. The derivatives of $p_{\varphi_l}(k\tilde{r})$ can be computed by chain rule as:

$$\begin{Bmatrix} \partial/\partial x \\ \partial/\partial y \end{Bmatrix} \overline{p}(\phi) = \begin{Bmatrix} \partial/\partial \overline{x} \\ \partial/\partial \overline{y} \end{Bmatrix} \exp[\, i(k\overline{x}\cos\phi + k\overline{y}\sin\phi)\,] = ik\exp[\, i(k\overline{x}\cos\phi + k\overline{y}\sin\phi)\,] \begin{Bmatrix} \cos\phi \\ \sin\phi \end{Bmatrix} \quad (40)$$

5.2 Eight-Node Quadrilateral Element P8

The eight-node element needs at least eight domain modes to secure the rank sufficiency. Starting from the plane wave modes in (39), the two wave propagation directions bisecting those of (39) can be included. In other words, the following eight modes are employed:

$$\{\overline{p}(\theta_2+\frac{\pi}{2}), \overline{p}(\theta_3-\frac{\pi}{2}), \overline{p}(\frac{\theta_2+\theta_3}{2}), \overline{p}(\frac{\theta_2+\theta_3}{2}+\frac{\pi}{2})\} = \{\mathrm{Re}(\overline{p}(\theta_2+\frac{\pi}{2})), \mathrm{Im}(\overline{p}(\theta_2+\frac{\pi}{2})), \mathrm{Re}(\overline{p}(\theta_3-\frac{\pi}{2})),$$

$$\mathrm{Im}(\overline{p}(\theta_3-\frac{\pi}{2})), \mathrm{Re}(\overline{p}(\frac{\theta_2+\theta_3}{2})), \mathrm{Im}(\overline{p}(\frac{\theta_2+\theta_3}{2})), \mathrm{Re}(\overline{p}(\frac{\theta_2+\theta_3}{2}+\frac{\pi}{2})), \mathrm{Im}(\overline{p}(\frac{\theta_2+\theta_3}{2}+\frac{\pi}{2}))\} \quad (41)$$

The resulting element has been verified to be rank sufficient and invariant. It will be termed as P8. Note worthily, the two directions bisecting the element diagonals have been employed by MacNeal to secure the invariance of an assumed strain shell element [28,30].

6. NUMERICAL EXAMPLES

Predictions of the following Q4 (four-node quadrilateral) and Q8 (eight-node quadrilateral) element models will be presented and discussed in this section:

C4 – the conventional Q4 element, see (6).

J4 or Q4-J4– the hybrid Q4 element with 4 domain modes from the Bessel solution set, see (28).

J5 or Q4-J5– the hybrid Q4 element with 5 domain modes from the Bessel solution set, see (26).

P4 – the hybrid Q4 element with 4 plane-wave domain modes, see (39).

C8 – the conventional Q8 element, see (6).

C8(2) – the conventional Q8 element which is evaluated by the second order quadrature, see (6).

J8 or Q8-J8– the hybrid Q8 element with 8 domain modes from the Bessel solution set, see (33).

J9 or Q8-J9– the hybrid Q8 element with 9 domain modes from the Bessel solution set, see (32).

P8 – the hybrid Q8 element with 8 domain modes from the plane wave solution set, see (41).

Unless stated otherwise, the matrices for the four-node and eight-node elements are evaluated by the second and third order quadratures, respectively.

When exact solution u^{exact} of a problem exist, the following normalized error will be computed for the conventional elements:

$$\text{normalized error} = \frac{\| u - u^{exact} \|}{\| u^{exact} \|} = \frac{\left(\int_{\Omega} \left(u - u^{exact} \right)^2 d\Omega \right)^{1/2}}{\left(\int_{\Omega} \left(u^{exact} \right)^2 d\Omega \right)^{1/2}} = \frac{\left(\sum_e \int_{\Omega^e} \left(u - u^{exact} \right)^2 d\Omega \right)^{1/2}}{\left(\sum_e \int_{\Omega^e} \left(u^{exact} \right)^2 d\Omega \right)^{1/2}} \quad (42)$$

where u denotes the finite element prediction. In the hybrid-Trefftz elements, u is the prediction along the element boundary and g is the prediction within the element domain. Hence, the above normalized error is modified to be

$$\text{normalized error} = \frac{\| g - u^{exact} \|}{\| u^{exact} \|} = \frac{\left(\int_{\Omega} \left(g - u^{exact} \right)^2 d\Omega \right)^{1/2}}{\left(\int_{\Omega} \left(u^{exact} \right)^2 d\Omega \right)^{1/2}} = \frac{\left(\sum_e \int_{\Omega^e} \left(g - u^{exact} \right)^2 d\Omega \right)^{1/2}}{\left(\sum_e \int_{\Omega^e} \left(u^{exact} \right)^2 d\Omega \right)^{1/2}} \quad (43)$$

In (42) and (43), the domain integrations are evaluated by using the same order of quadrature as for evaluating the element matrix. (42) is also evaluated for the hybrid-Trefftz element using nodal integration in which the sampling points of the integrand are the nodes. The normalized error for g and the nodal integrated error for u are exceptionally close and graphically indistinguishable. Hence, the latter will not be separately shown for graphical clarity. Furthermore, the following parameter will be employed to quantity the mesh or nodal density with respect to the wavelength:

$$N_n = \text{wave length / nodal spacing} = 2\pi / (kh) \quad (44)$$

For conventional element models, 10 or above being the recommended value of N_n can be noted in the literature (see, e.g., [21]).

6.1 Condition Number versus Integration Order

The single element problem in Figure 3 is considered. The element edge lengths are 1, √5, √10 and √10. For the four-node and eight-node elements, the average nodal spacings are 2 and 1 whilst the wavenumbers are taken to 1/4 and 1/2, respectively. The chosen wavenumber will lead to $N_n \approx 2\pi$. Let α denote the eigenvalue of the element matrix, $|\alpha|_{max}$, $|\alpha|_{min}$ and the condition number N_c (= $|\alpha|_{max}/|\alpha|_{min}$) are computed and listed in Table 1 when the element matrices are evaluated by various orders of quadrature.

Four-node Elements – All the four-node elements are rank deficient ($N_c = \infty$) when the first order quadrature is employed. On the order hand, the changes in N_cs are less than 1.8% when second or higher order quadratures are used. In this light, second order quadrature will be employed for evaluating the element matrices and the normalized errors of all four-node elements. It is also checked that their predictions remain practically constant when the third or higher order quadrature rule is employed.

Table 1. $|\alpha|_{max}$, $|\alpha|_{min}$ and N_c of the elements ($N_n \approx 2\pi$) under different orders of quadrature.

	2nd order quadrature			3rd order quadrature			4th order quadrature			5th order quadrature		
	$\|\alpha\|_{max}$	$\alpha\|_{min}$	N_c	$\|\alpha\|_{max}$	$\alpha\|_{min}$	N_c	$\|\alpha\|_{max}$	$\alpha\|_{min}$	N_c	$\|\alpha\|_{max}$	$\alpha\|_{min}$	N_c
C4*	1.563	0.315	4.955	1.591	0.315	5.043	1.593	0.315	5.050	1.591	0.315	5.049
J4*	1.473	0.335	4.394	1.471	0.335	4.391	1.471	0.335	4.391	1.471	0.335	4.391
J5*	1.473	0.335	4.397	1.471	0.335	4.393	1.471	0.335	4.393	1.471	0.335	4.393
P4*	1.456	0.336	4.337	1.454	0.335	4.336	1.454	0.335	4.336	1.454	0.335	4.336
C8	6.482	0.175	37.06	6.859	0.175	39.16	6.870	0.175	39.23	6.853	0.175	39.17
J8	---	0	∞	3.211	0.173	18.54	3.212	0.177	18.15	3.212	0.177	18.15
J9	---	0	∞	3.211	0.179	17.94	3.212	0.179	17.92	3.212	0.179	17.92
P8	---	0	∞	3.211	0.179	17.90	3.211	0.179	17.89	3.211	0.179	17.89

* Under the first order quadrature, N_c of all four-node elements are equal to ∞.

Eight-node Elements – Among the eight-node elements, only the conventional element C8 is rank sufficient when the second order quadrature is employed. However, N_c of C8 changes by nearly 5.7% when the quadrature order switches from second to third. On the order hand, the difference in N_c of all the hybrid-Trefftz elements are less than 2.2% when the third or higher order quadratures are used. Unless otherwise specified, the third order quadrature will be employed for all eight-node elements. Their predictions remain practical constant when the fourth or higher order quadrature rule is employed. It will also be seen in some examples that C8, which is evaluated by the third order quadrature, is considerably more accurate than its counterpart C8(2) evaluated by the second order quadrature.

6.2 Invariant Tests

The single element problem in Figure 3 is also employed for the invariant tests. All elements are translated in the *x*-*y*-plane and rotated about A. Different connectivity is also attempted. Under all settings, all the element eigenvalues remain unchanged. The invariance (comprising translational, rotational and connectivity invariance) of all elements are confirmed.

6.3 Plane Wave Problem modeled by Square Elements

Figure 4a depicts a $L \times L$ problem domain modelled by 4×4 square elements and L is set to be 2. The domain boundary is prescribed with the natural boundary condition with respect to to the following plane wave solution:

$$u^{\text{exact}} = \cos(kx\cos\varphi + ky\sin\varphi) \tag{45}$$

where φ is the wave propagation direction. As the predictions exhibit a periodicity of 45°, only those for $0° \le \varphi \le 90°$ are presented.

Four-node Square Elements - Figure 5 shows the normalized error versus φ for kL = 8, 12 and 16. The N_n-value is fixed at 2π by varying the mesh density. The data are computed at 5° interverl of φ. As the elements are square in shape, the predictions of J4 and J5 are identical. On the other hand, J4/J5 and P4 produce graphically indistinguishable results which are not separately presented in the figure for clarity. By normalizing the average errors of J4/J5/P4 with those of C4, one gets 56%, 51% and 79% for kL equal to 8, 12 and 16, respectively. Figure 6 plots the normalized error versus φ by fixing kL at 8. Three different meshes which lead to N_n = 2π, 3π and 4π are considered. Convergence is obvious. By normalizing the average errors of J4/J5/P4 with those of C4, one gets 56%, 52% and 51% for N_n equal to 2π, 3π and 4π, respectively. Figure 7 shows another convergence study in which kL is raised to 16. As the previous normalized errors attain their maximum or minimun at φ = 0° or 45°, the predictions at two intermediate propagation directions given by φ = 15° and 30° are considered. The range of N_n is wide and it covers from 2π to 24.5π. All elements are markedly more accurate when φ = 30°. In Figures 5 to 7, the hybrid four-node elements are consistently more accurate than their convenctional counterpart.

Eight-node Square Elements - Figure 8 shows the normalized error versus φ for kL = 8, 12 and 16. The N_n-value is again fixed to 2π. As the elements are square in shape, the predictions of J8 and J9 are identical. On the other hand, J8/J9 and P8 produce graphically indistinguishable results which are not separately presented in the figure for clarity. By normalizing the average errors of J8/J9/P8

with those of C8, one gets 17%, 8% and 29% for kL equal to 8, 12 and 16, respectively. Figure 9 plots the normalized error versus φ by fixing kL to 8. Three meshes with $N_n = 2\pi$, 3π and 4π are considered. Convergence is apparent. By normalizing the average errors of J8/J9/P8 with those of C8, one gets 17%, 14% and 11% for N_n equal to 2π, 3π and 4π, respectively. Figure 10 shows another convergence study in which kL is raised to 16. As the previous normalized errors attain their maximum or minimun when φ is close to 0° or 45°, the predictions at two intermediate propagation directions given by φ = 15° and 30° are considered. The range of N_n is wide and spans from 2π to 12π. Unlike Figure 7 for the four-node elements, the vertical axis is on logarithmic scale as the normalized error varies from 0.01% to 100%. All elements are markedly more accurate at φ = 30°. To avoid compressing the ordinate, the error of C8(2) which is evaluated by the second order quadrature and is considerable larger than that of C8 is not included in Figures 8 and 9 but only in Figure 10. Except at the left end of the abscissa, it can be seen that the error of C8(2) is roughly 80% larger than that of C8. In Figures 8 to 10, the hybrid eight-node elements are consistently more accurate than their convenctional counterpart.

Given the same N_n or nodal spacing per wavelength, it can be seen in this series of examples that C4 and C8 yield similar accuracy whislt the hybrid Q8 elements are markedly more accurate than the hybrid Q4 elements.

6.4 Plane Wave Problem modeled by Rectangular Elements

This subsection study the effect of non-square element geometry on the elemen predictions using the previous plane wave problem. Figure 4b depicts the problem domain modelled by 8×4 rectangular elements.

Four-node Rectangular Elements – Figure 11 plots the normalized errors versus φ for the element aspect ratios 2 and 4 which are realized by modelling the problem domain with 16×8 and 16×4 four-node elements, respectively. Furthermore, kL is set to be 8 for limiting the maximum normalized error to 50%. All elements are most accurate at φ = 0°/180° and most erroneous at around φ = 90°. The observations are understandable as nodal spacing is shortest and longest along φ = 0°/180° and 90°, respectively. By normalizing the average errors of hybrid four-node elements with those of C4 (see Figure 6 and Figure 11), one gets 51%, 59% and 37% when 16×16 (aspect ratio = 1), 16×8 (aspect ratio = 2) 16×4 (aspect ratio = 4) elements are employed, respectively. For most values of φ in Figure 11, J4 is more accurate than J5/P4.

Eight-node Rectangular Elements – Figure 12 plots the normalized errors versus φ for the element aspect ratios 2 and 4 which are realized by modelling the problem domain with 8×4 and 8×2

eight-node elements, respectively. kL is again set to be 8 for limiting the maximum normalized error to 50%. Again, all elements are most accurate at φ = 0°/180° and most erroneous at around φ = 90°. By normalizing the average errors of hybrid eight-node element with those of C8 (see Figure 9 and Figure 13), one gets 11%, 42% and 64% when 8×8 (aspect ratio = 1), 8×4 (aspect ratio = 2) 8×2 (aspect ratio = 4) element are are employed, respectively. Unlike the four-node elements, the eight-node hybrid elements are less and less accurate with respect to the eight-node conventional element when the aspect ratio increases.

All elements are adversely affected when the aspect ratio departs from unity. Neverthelss, the hybrid elements remain to be consistently more accurate than the conventional elements.

6.5 Plane Wave Problem modeled by Skew Elements

This subsection study the effect of element skewness on the predictions using the plane wave problem. Figure 4c depicts the $L\times L$ problem domain modelled by 4×4 skew elements. Here, an element is said to be a skew one if any pair of its opposite edges are non-parallel. Two skewed meshes with $4e/L$ = 0.16 and 0.32 are considered. Noteworthily, some elements would possess convex interior corners and negative Jacobian determinants when $4e/L > 0.5$. The skewness implied by $4e/L$ = 0.32 is indeed unrealistically severe and are always avoided in practice.

Four-node Skew Elements – Figure 13 plots the normalized errors versus φ when the problem domain is modelled by 16×16 four-node elements which are obtained by subdividing each of the 4×4 elements in Figure 4(c) into 4×4 elements. Inheriting from the last subsection, kL is again set to be 8 which leads to $N_n \approx 4\pi$. At the chosen kL and mesh density, the conventional elements are most erroneous and accurate at φ = 45° and 0°/90°, respectively. Conversely, the hybrid elements are most erroneous and accurate at φ = 0°/90° and 45°, respectively. By normalizing the average errors of hybrid elements with those of C4 (see Figure 6 and Figure 13), one gets 51%, 53% and 51% for $4e/L$ equals 0, 0.16 and 0.32, respectively. J4 is sometimes more accurate than J5/P4 and vice versa.

Eight-node Skew Elements – The problem domain is now modelled by 4×4 eight-node elements as shown in Figure 4c. kL is again set to be 8 which leads to $N_n \approx 2\pi$. The combination of kL and mesh density is chosen such that the maximum error of conventional element is limited to 50% as in Figure 13. Figure 14 plots the normalized errors versus φ for the eight-node elements. The conventional elements are most accurate at φ = 45° and 0°/90°. On the other hand, the hybrid elements are most erroneous and accurate at φ = 0°/90° and 45°, respectively. By normalizing the average errors of hybrid elements with those of C8 (see Figure 9 and Figure 14), one gets 14%, 22%, 43% for $4e/L$ = 0, 0.16 and 0.32, respectively. Unlike the four-node elements, the eight-node

hybrid elements are less and less accurate with respect to the eight-node conventional element when the aspect ratio increases.

All elements are adversely affected by the geometric skewness. Neverthelss, the hybrid elements are consistently more accurate than the conventional elements.

6.6 Quarter Circular Panel Problem

Figure 15 shows a quarter of a circular panel of unit radius modeled by n (= 8) elements along each coordinate axis. It can be seen that all elements are only mildly distorted. The exact solution of this problem is:

$$u^{\text{exact}} = 2\frac{J_2(kr)}{J_2(k)}\cos 2\theta \tag{46}$$

Natural boundary condition is prescribed along the entire boundary of the panel. In this example, the normalized errors are computed for $5 \le kR \le 20$ whilst the mesh densities are selected such that N_n falls roughly in between 10 and 20. The predictions of J5 and P4 are graphically indistinguishable and would not be plotted separately for clarity. On the other hand, the predictions of J8, J9 and P8 are graphically indistinguishable and would not be plotted separately for clarity.

Four-node Elements – Figure 16 plots the normalized error for $5 \le kR \le 10$ in an increment of 0.25. With 16 elements along the coordinate axis, $N_n \approx 20$ and 10 when kR = 5 and 10, respectively. The average errors of J4, J5/P4 and C4 are in the ratio of 30% : 31% : 100%. C4 is consistently less accurate than the hybrid elements. Figure 17 plots the normalized error for $10 \le kR \le 20$ at increments of 0.5. With 32 elements along the coordinate axis, $N_n \approx 20$ and 10 when kR = 10 and 20, respectively. The ratio of the averaged errors of J4, J5/P4 and C4 is 45% : 46% : 100%. C4 is consistently less accurate than the hybrid elements except at kR = 16 and 19.5 where all elements exhibit error peaks. Figures 16 and 17 show that all the hybrid elements are close in accuracy. At some values of kR, J4 is marginally more accurate than J5/P4 and vice versa.

Eight-node Elements – Figure 18 plots the normalized error for kR from 5 to 10 in an increment of 0.25. With 8 elements along the coordinate axis, $N_n \approx 20$ and 10 when kR = 5 and 10, respectively. The averaged errors of J8/J9/P8, C8(2) and C8 are in the ratio of 20% : 172% : 100%. Figure 19 plots the normalized error for kR from 10 to 20 in the increment of 0.5. With 16 elements along the coordinate axis, $N_n \approx 20$ and 10 when kR = 10 and 20, respectively. The average errors of J8/J9/P8, C8(2) and C8 are in the ratio of 23% : 180% : 100%. From the present problem and the last plane wave problem, the error of C8(2) is 60%~80% larger than that of C8. Though the second

order quadrature is computationally more efficient and C8(2) is rank sufficient, the integration scheme is highly detrimental to the element accuracy. In Figures 18 and 19, the hybrid elements are consistenly more accuracy than the conventional elements.

6.7 Square Panel with a Circular Cutout

A 10×10 square panel with a $\phi 2$ circular cutout is portrayed in Figure 20. Its left-hand and right-hand edges are prescribed with $u = 1$ and 0, respectively, whilst $u_{,n} = 0$ along the boundary of the $\phi 2$ circular cutout, the top and bottom edges. Owing to symmetry, only half of the domain is modeled and meshed into $n \times 2n$ elements whilst $u_{,n} = 0$ is prescribed along AB and DE. Unlike the last example, the present problem contains considerably distorted elements. In particular, the aspect ratio of the elements along the problem domain boundaries A-F-G-E and BCD are roughly 2.5. The predictions along ABCDE are plotted against $s \in [0,8+\pi]$ which is the length coordinate along ABCDE. The N_n-value will be calculated as the wavelength divided by $\sqrt{A}$ and $(\sqrt{A})/2$ for the four-node and eight-node elements, respectively, in which A denote the average area of the element. Results for k equal to 2, 4 and 6 are computed. Highly converged solutions have been computed for reference.

Four-node Elements – Figures 21, 22 and 23 show the predictions. The N_n-value is kept constant at 40.9 which is yielded by using 64×128, 128×256 and 192×384 four-node elements for k equal to 2, 4 and 6, respectively. The combinations of N_n and k are chosen such that predictions of the hybrid elements vary from accurate at k =2 to erroneous at k = 6. The "dispersion" effect is more obvious at higher k [31]. All hybrid elements are markedly more accurate than C4 which is erroneous even at k = 2. "Dispersion" effect in C4 is also obvious at higher k. Note worthily, J4 is markedly more accurate than J5/P4 in this problem which is modeled by considerably distorted meshes.

Eight-node Elements – Figures 24, 25 and 26 show the predictions. The N_n-value is kept constant at 12.8 which is yielded by using 10×20, 20×40 and 30×60 eight-node elements for k equal to 2, 4 and 6, respectively. Again, the combinations of N_n and k are chosen such that predictions of the hybrid elements vary from accurate at k =2 to erroneous at k = 6. All hybrid elements are markedly more accurate than C8 which is erroneous even at k = 2. "Dispersion" effect in C8 is also obvious at higher k. J8 is marginally more accurate than J9/P8.

In this example, the mesh distortion is characterized by fairy large element aspect ratios and small skewness. The observation that J4 and J8 are more accurate than J5 and J9, respectively, echoes the

results presented in Section 6.5.

6.8 Effect of Additional Domain Approximation Modes

It has been mentioned in Section 4 that the optimal number of stress modes in the hybrid stress element is often considered to be the same as the minimal number of stress modes required for securing the element rank sufficiency. When the plane wave problem is modeled by square elements (see Figure 4a), the four-node or Q4 hybrid elements yield exceptionally close predictions in mildly distorted mesh. The same observation applies to the eight-node or Q8 hybrid-Trefftz elements. Hence, the square mesh would be the best choice for examining the effect of including additional domain approximation modes into the elements. In this light, Q4-J7, Q4-J9, Q8-J11 and Q8-J13 are implemented. Their shape function matrices of the domain approximation modes are obtained by augmenting the five-mode matrix in (26) with increasing number pairs of terms of the form $[J_m(k\tilde{r})\cos m\tilde{\theta}, J_m(k\tilde{r})\sin m\tilde{\theta}]$ where m = 3, 4, 5 and 6. The matrices (**G** and **H**) of the four elements are computed by the second, third, third and fourth order quadratures, respectively. Any lower order integration rule would lead to rank deficient elements. All elements are invariant. Their accuracy and convergence are studied by the plane wave problem with the wave propagation direction angles φ set at 15° and 30°.

Four-node Elements – Figure 27 shows the results for the four-node hybrid-Trefftz elements. As the problem is modeled by square elements, the predictions of Q4-J4 and Q4-J5 are identical. Elements Q4-J4/Q4-J5 and Q4-J4/Q4-J5/Q4-J7 yield close prediction which, however, are slightly more accurate than Q4-J9.

Eight-node Elements – Figure 28 shows the results for the eight-node hybrid-Trefftz elements. As this problem employs only square elements, the predictions of Q8-J8 and Q8-J9 are identical. The two element models are markedly more accurate than Q8-J11 and Q8-J13.On the other hand, Q8-J11 is slightly more accurate than Q8-J13.

In all previous examples involving distorted elements, Q4-J4 and Q8-J8 are mostly more accurate and sometimes markedly more accurate than Q4-J5 and Q8-J9, respectively. It only happens occasionally that Q4-J5 and Q8-J9 are marginally more accurate than Q4-J5 and Q8-J8, respectively. These examples together with the present one support the use of minimal number of domain modes from accuracy point of view. From computational point of view, using the minimal number of domain modes is advantageous for reducing the cost in matrix manipulation and integration.

6.9 A Further Set of Problems on Effect of Mesh Distortion

This set of problems are protrayed in Figures 29(a) to (c). They are suggested by a reviewer for further studying the effect of mesh distortion which is characterized by "e" varying from 0 to 0.5. Boundary conditions with respect to the plane wave propagating at $\varphi = \pi/8$ (see (45)) are adopted. For the domain edges along which the nodal spacings are identical, natural boundary conditions are prescribed. For the remaining edges, essential boundary conditions are presribed. In other words, both essential and natural boundary conditions are used in the same mesh. In (a) and (b), 8×8 nodal spacings are employed. In (c), 16×4 nodal spacings are employed. With $k = 2$, the average N_n equals 4π. The N_n is chosen such that the the largest normalized errors of the two conventional elements C4 and C8 are about 10% which occurs in (c) for both elements. Figures 30, 31 and 32 plot the normalized errrors versus "e" for the four-node elements in (a), (b) and (c), respectively. The errors of J5 are always between those of P4 and J4 and, thus, are not included in the figures for clarity. The hybrid elements produce very close results with J4 being the most accurate one among them. Their errors are roughly 30~50% of their conventional counterpart. Figures 33, 34 and 35 show the normalized errrors versus "e" for the eight-node elements in (a), (b) and (c), respectively. The errors of J9 are always between those of P8 and J8 and, thus, are not included in the figures for clarity. The hybrid elements produce very close results with J8 being the most accurate one among them. Their errors are roughly 10~30% of their conventional counterpart.

As a matter of fact, results for $\varphi = 0$ and $\pi/4$ are also computed. For the two directions, the error ratio of hybrid to conventional elements are lower than those for $\varphi = \pi/8$. In other word, the relative accuracy of the hybrid elements with respect to the conventional are higher. The results are not shown to save page length.

7. CLOSURE

Plane four-node and eight-node hybrid-Trefftz elements are devised in this paper. They have the same boundary (nodal, frame or inter-element) degrees of freedom as the conventional single-field elements and can be readily be incorporated into the standard finite element program framework. Both the Bessel and plane wave solution sets are employed in constructing the domain (or intra-element) approximation space. By using local coordinate systems and directions, the new elements are invariant and possess the minimal numbers or one additional domain approximation modes for rank sufficiency of the element matrices. The examples are affirmative to the use of minimal number of domain modes for higher accuracy. From computational point of view, using the minimal number of domain modes is also advantageous for reducing the cost in matrix manipulation and integration.

In absolute majority of the examples, the hybrid-Treffty elements are markedly more accurate than the conventional single-field elements of the same nodal configurations. When the elements are close to square in shape, the proposed hybrid-Treffty elements with the same nodal configuration yield close solutions. However, when distorted elements are employed, the elements employing the minimal numbers of Bessel modes are more accurate than their counterparts that employ additional numbers of Bessel modes and minimal numbers of plane wave modes.

Mesh distortion sensitivity is studied by using slender and skew mesh geometry. All elements are adversely affected by the distortion. Judging from the ratios of the normalized errors of the hybrid-Trefftz and conventional elements, the normalized accuracy of the hybrid four-node elements with respect to that of the conventional four-node element does not drop when the mesh distortion increases. On the other hand, the normalized accuracy of the hybrid eight-node elements with respect to that of the conventional eight-node element drops when the mesh distortion increases but the deterioration is trivial only when mesh distortion is considerably severe. Unlike the finite deformation solid mechanics problem in which the mesh deforms with the solid, severe distortion in static meshes can readily be avoided by mildly experienced finite element practitioners and even the most affordable quad-mesh generation software. Most importantly, the hybrid-Trefftz elements still surpass the conventional elements even when the mesh distortion is impractically severe.

Same as the hybrid-stress elements, the use of domain approximations in the present hybrid-Trefftz elements cannot improve the rate of convergence (see Figure 7 and 10) which is controlled by the nodal interpolation order. In examples where the conventional element can yield moderate predictions (e.g. < 20%), the errors of four-node hybrid-Trefftz elements are typically 40~50% of their conventional counterpart whereas the errors of eight-node hybrid-Trefftz elements are typically 10~20% of their conventional counterpart. The improvement in accuracy can justify the higher computational cost of the hybrid-Trefftz elements as the overall computational cost for moderate and large problems is dominated by the matrix solution time [28].

Finally, the proposed elements are not expected to cope with problems (such as those with high *k*-values) which cannot be coped with by the conventional single-field elements. Given a problem which can be tackled by the conventional elements, the proposed elements can provides considerably more accurate solutions than the conventional elements.

Acknowledgement – This work is funded by the *Research Grant Council of Hong Kong* under grant HKU 716708E. The correspondence author is grateful to Professor Isaac Harari for the useful discussions during the Trefftz 2008 Workshop held in Leuven, Belgium. Special thanks are given to

the reviewers whose comments and suggestions are valuable for enhancing the quality of this paper.

REFERENCES

[1] Pian THH. Derivation of element stiffness matrices by assumed stress distribution. *J.AIAA* **2**: 1332-1336 (1964)

[2] Tong P, Pian THH, Lasry SL. A hybrid-element approach to crack problems in plane elasticity. *Int.J.Numer.Meth.Engng.* **7**: 297-308 (1973)

[3] Atluri SN, Kobayashi AS, Nakagaki M. An assumed displacement hybrid finite element method for fracture mechanics. *Int.J.Fracture* **11**: 257–271 (1975)

[4] Pian THH. State-of-the-art development of hybrid/mixed finite element method. *Finite Elements in Analysis & Design* **21**: 5-20 (1995)

[5] Sze KY, Chan WK, Pian THH. An eight-node hybrid-stress solid-shell element for geometric nonlinear analysis of elastic shells. *Int.J.Numer.Meth.Engng.* **55**: 853-878 (2000)

[6] Jirousek J. Basis for development of large finite elements locally satisfying all field equations. *Comput.Meth. Appl.Mech.Engng.* **14**: 65-92 (1978)

[7] Jirousek J, Zieliński AP. Survey of Trefftz-type element formulations. *Computers & Structures* **63**: 225-242 (1997)

[8] Freitas JA, Almeida JP, Pereira EMB. Non-conventional formulations for the finite element method. *Comput.Mech.* **23**: 488-501 (1999)

[9] Qin QH. Solving anti-plane problems of piezoelectric materials by the Trefftz finite element approach. *Comput.Mech.* **31**: 461-468 (2003)

[10] Wang HT, Sze KY, Yang XM. Analysis of electromechanical stress singularity in piezoelectrics by computed eigensolutions and hybrid-trefftz finite element models. *Comput. Mech.* **38**: 551–564 (2006)

[11] Zielinski AP, Herrera I. Trefftz method: fitting boundary conditions. *Int.J.Numer.Meth.Engng.* **24**: 871-891 (1987)

[12] Cheung YK, Jin WG, Zienkiewicz OC. Solution of Helmholtz equation by Trefftz method. *Int.J.Numer. Meth.Engng.* **32** 63–78 (1991)

[13] Herrera I. Trefftz method: A general theory. *Numerical Meth.for Partial Differential Equations* **16**: 561-580 (2000)

[14] Sladek J, Sladek V, Keer RV. Global and local Trefftz boundary integral formulations for sound vibration. *Advances in Engineering Software* **33**: 469-476 (2002)

[15] Chang JR, Liu RF. An asymmetric indirect Trefftz method for solving free-vibration problems. *J. Sound & Vibration* **275**: 991–1008 (2004)

[16] Stojek M. Least square Trefftz-type elements for the Helmholtz equation. *Int.J.Numer.Meth. Engng.* **41**: 831-849 (1998)

[17] Stojek M, Markiewicz M, Mahrenholtz O. Diffraction loads on multiple vertical cylinders with rectangular cross section by Trefftz-type finite elements, *Computers & Structures* **75**: 335-345 (2000)

[18] Freitas JAT, Cismaşiu C. Hybrid-Trefftz displacement element for spectral analysis of bounded and unbounded media. *Int.J.Solids & Structures* **40**: 671-699 (2003)

[19] Melenk JM, Babuška I. The partition of unity method. *Int.J.Numer.Meth.Engng.* **40**:727 – 758 (1997)

[20] Mayer P, Mandel J. The finite ray element method for the Helmholtz equation of scattering: first numerical experiments. *Report 111*, Center of Computational Mathematics, University of Colorado at Denver, 1997.

[21] Laghrouche O, Bettess P. Short wave modelling using special finite elements. *J. Computational Acoustics* **8**: 189-210 (2000).

[22] Ortiz P, Sanchez E. An improved partition of unity finite element method for diffraction problems. *Inter.J.Numer.Meth.Engng.* **50**:2727 – 2740 (2001).
[23] Farhat C, Harari I, Hetmaniuk U. The discontinuous enrichment method for multiscale analysis. *Computer Meth.in Appl.Mech. & Engng.* **192**: 1389-1419 (2003)
[24] Farhat C, Harari I, Hetmaniuk U. A discontinuous Galerkin method with Lagrange multipliers for the solution of Helmholtz problems in the mid-frequency regime. *Computer Meth.in Appl.Mech. & Engng.* **192**: 3195-3209 (2003)
[25] Sze KY, Cheung YK. A hybrid-Trefftz finite element model for Helmholtz problem. *Comm. Numer.Meth.Engng.* **24**: 2047-2060 (2008)
[26] Spilker RL, Maskeri SM, Kania E. Plane isoparametric hybrid-stress elements: invariance and optimal sampling. *Int.J.Numer.Meth.Engng.*, **17**, 1469-1496 (1981)
[27] Sze KY, Chow CL, Chen WJ. On invariance of isoparametric hybrid elements. *Commun. Numer.Meth.Engng.* **8**: 385-406 (1992)
[28] MacNeal RH. *Finite Elements: Their Design and Performance*. Marcel Dekker, Inc., 1994.
[29] Cook RD. Avoidance of parasitic shear in plane element", *ASCE J.Structural Engrg.* **101**: 1239-1253 (1975)
[30] MacNeal RH. Derivation of element stiffness matrices by assumed strain distributions. *Nuclear Engrg. & Design* **70**: 3-12 (1982)
[31] Deraemaeker A, Babuška I, Bouillard P. Dispersion and pollution of the fem solution for the Helmholtz equation in one, two and three dimensions. *Inter.J.Numer.Meth.Engng.* **46**: 471 – 499 (1999).

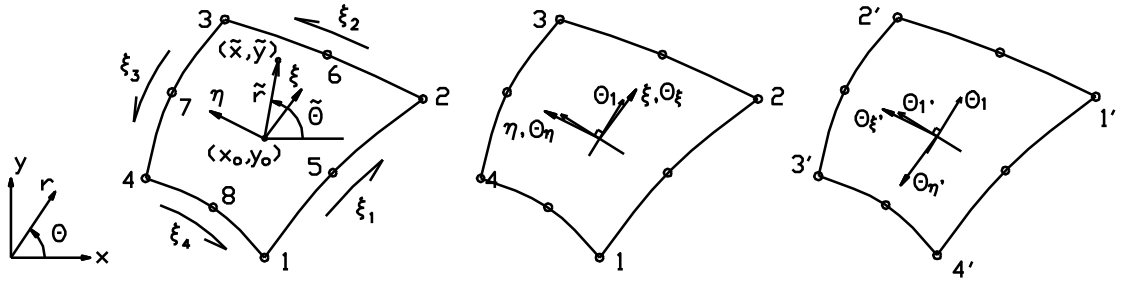

(a) (b) (c)

Figure 1. (a) The eight-node quadrilateral element, its parametric coordinates (ξ,η). ($\tilde{x},\tilde{y}$) and ($\tilde{r},\tilde{\theta}$) are the local coordinates defined with respect to the parametric origin (x_o,y_o). ξ_is are the four parametric boundary coordinates. (b) The local directions θ_ξ, θ_η and $\theta_1 = (\theta_\xi+\theta_\eta)/2 - \pi/4$. (c) Another set of local directions $\theta_{\xi'}$, $\theta_{\eta'}$ and $\theta_{1'} = (\theta_{\xi'}+\theta_{\eta'})/2 - \pi/4$) due to a change in element connectivity.

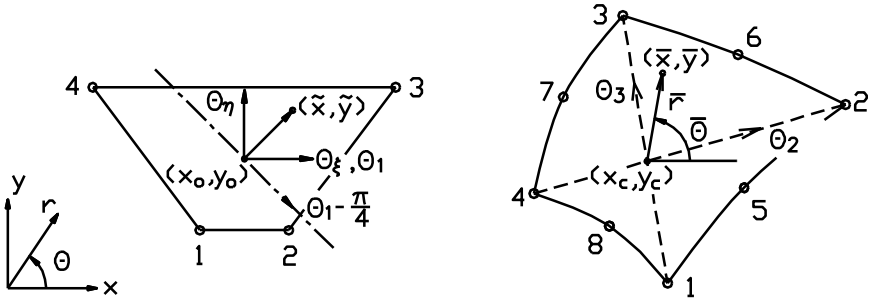

(a) (b)

Figure 2. (a) The wave crest — - — for the plane wave mode $\mathrm{Re}(\tilde{p}(\theta_1 + \pi/4))$ in a trapezoidal element. (b) The running directions (θ_2 and θ_3) along the element diagonals. ($\bar{x},\bar{y}$) and ($\bar{r},\bar{\theta}$) are local coordinates defined with respect to the intersection point (x_o,y_o) of the diagonals.

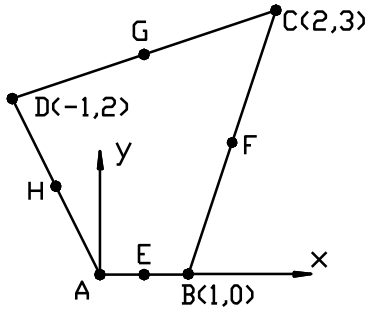

Figure 3. The single-element problem for examining the condition number and invariance of the element matrix. E, F, G and H are mid-edge nodes which appear only in the eight-node elements.

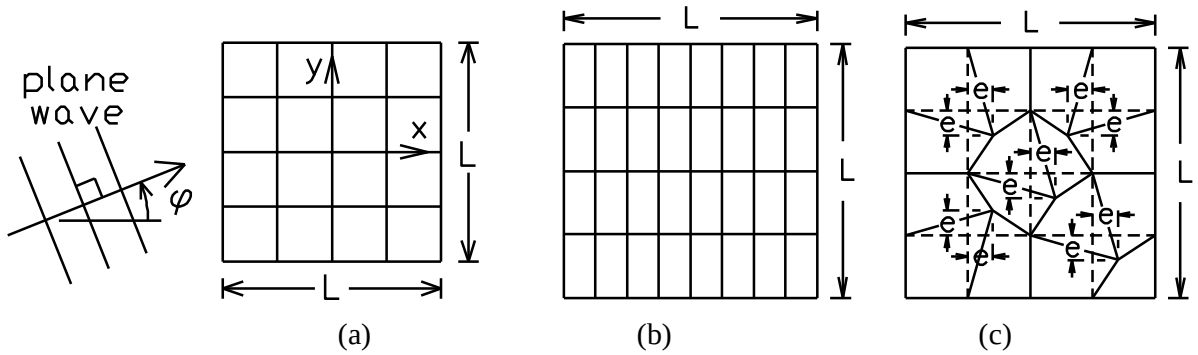

(a) (b) (c)

Figure 4. The plane wave problem in which exact solution is $u^{exact} = \cos(kx\cos\varphi + ky\sin\varphi)$. A $L \times L$ problem domain modeled by (a) 4×4 square elements, (b) 8×4 rectangular elements and (c) 4×4 skew elements.

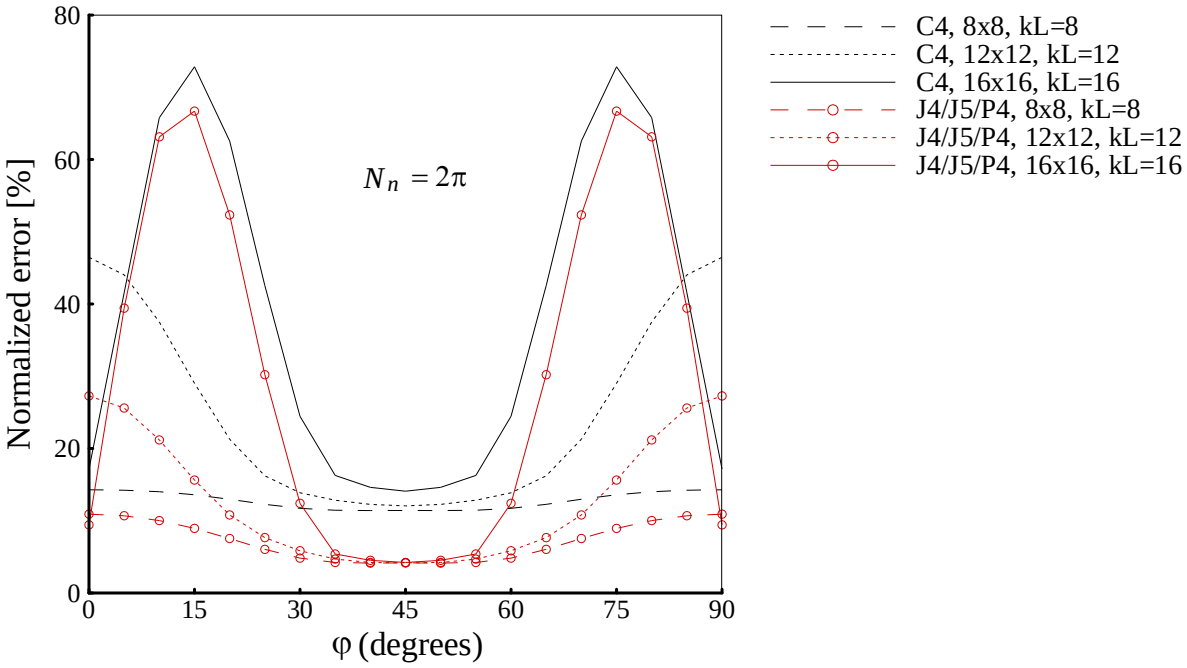

Figure 5. Normalized error of the four-node square elements for kL = 8, 12 and 16. The problem domain is modeled by 8×8, 12×12 and 16×16 elements, respectively, see Figure 4(a).

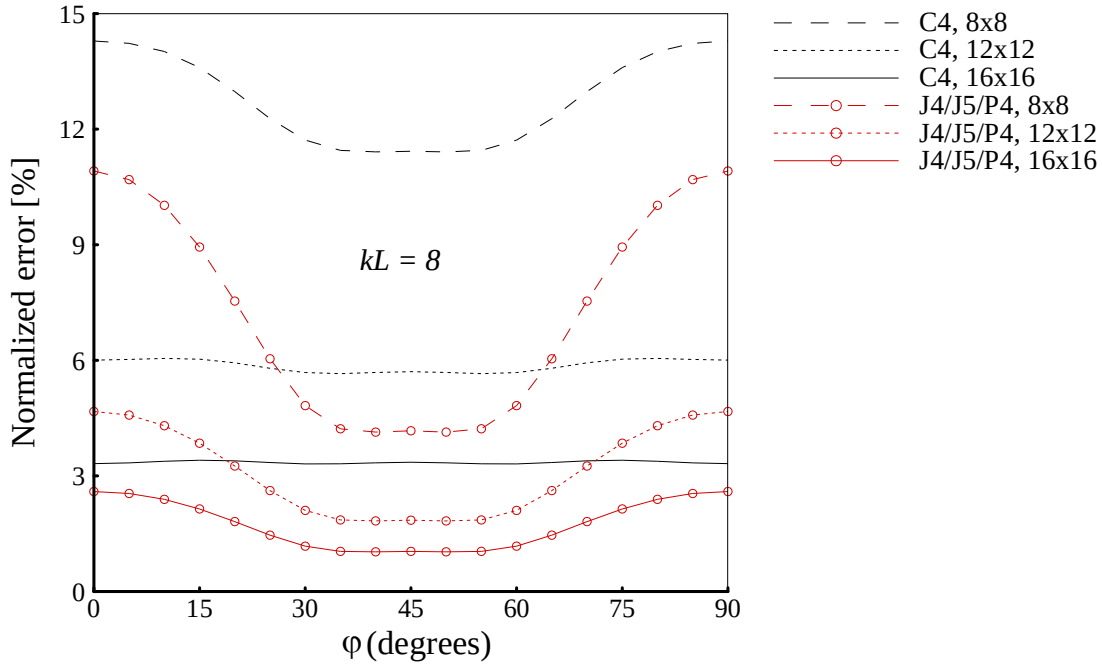

Figure 6. Normalized error of the four-node square elements for kL = 8. The problem domain is modeled by 8×8 ($N_n = 2\pi$), 12×12 ($N_n = 3\pi$) and 16×16 ($N_n = 4\pi$) elements, see Figure 4(a).

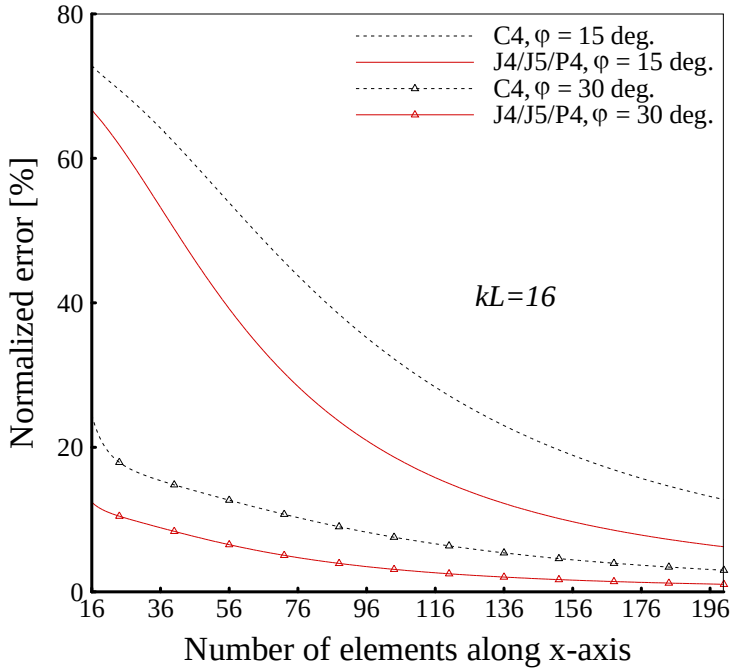

Figure 7. Convergence of the four -node square elements. When the number of element equals 16 and 196, N_n equals 2π and 24.5π, respectively, see Figure 4(a).

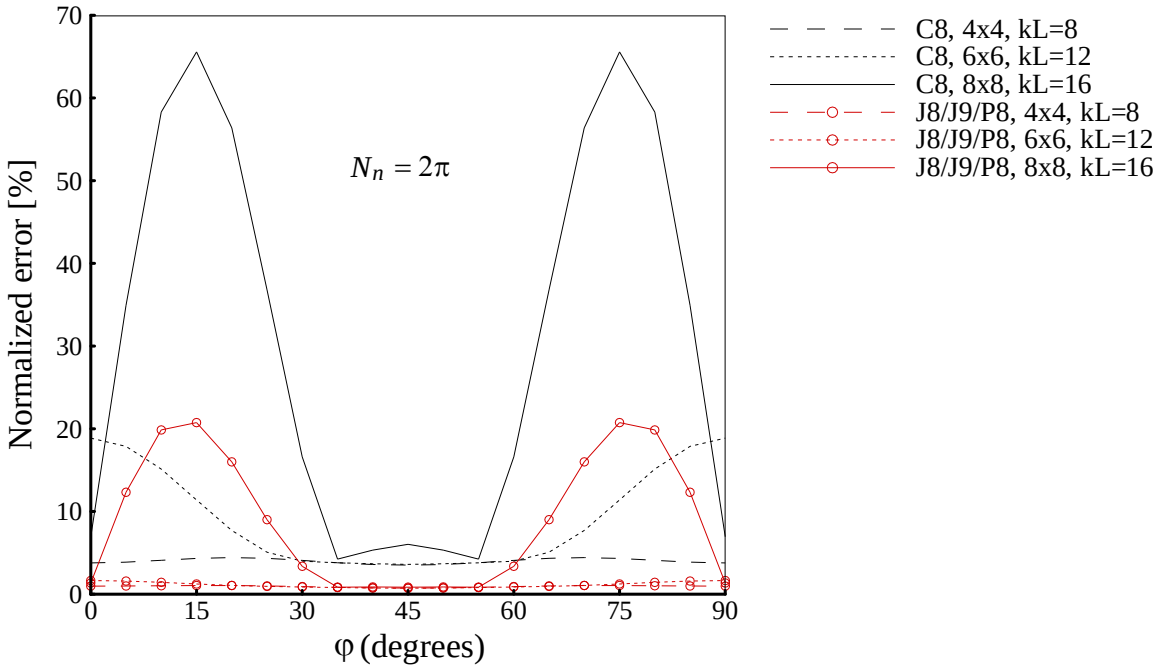

Figure 8. Normalized error of the eight-node square elements for *kL* = 8, 12 and 16. The problem domain is modeled by 4×4, 6×6 and 8×8 elements, respectively, see Figure 4(a).

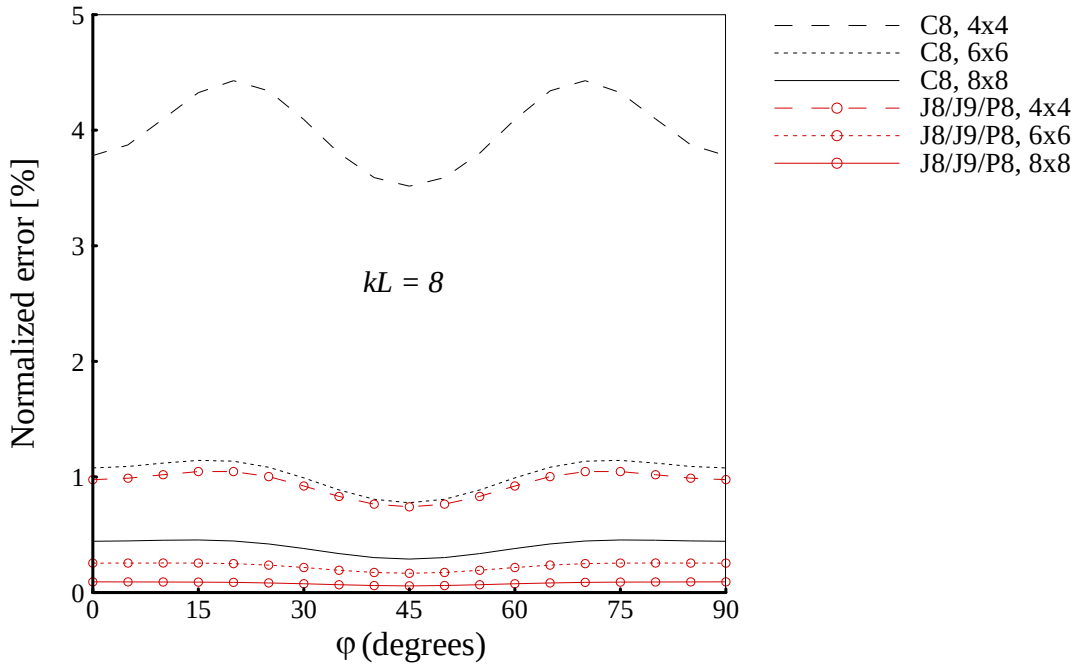

Figure 9. Normalized error of the eight-node square elements for $kL = 8$. The problem domain is modeled by 4×4 ($N_n = 2\pi$), 6×6 ($N_n = 3\pi$) and 8×8 ($N_n = 4\pi$) elements, see Figure 4(a).

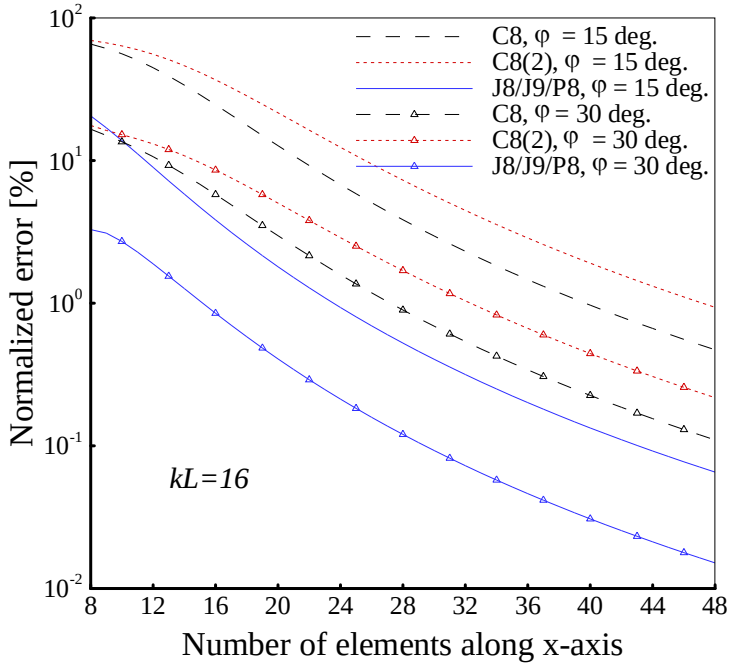

Figure 10. Convergence of the eight-node square elements. When the number of element equals 8 and 48, N_n equals 2π and 12π, respectively, see Figure 4(a).

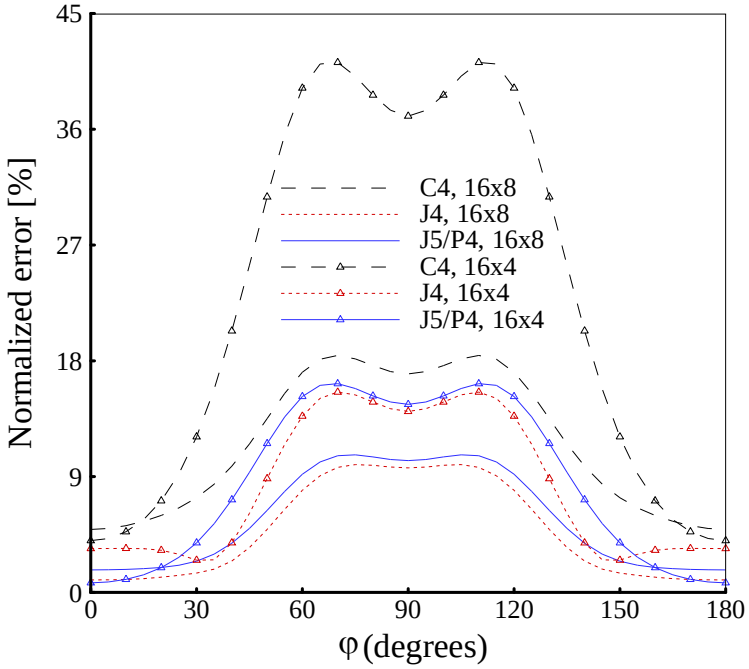

Figure 11. Normalized error of the four-node rectangular elements at aspect ratio 2 (16×8 elements) and 4 (16×4 elements) with kL = 8, see Figure 4(b).

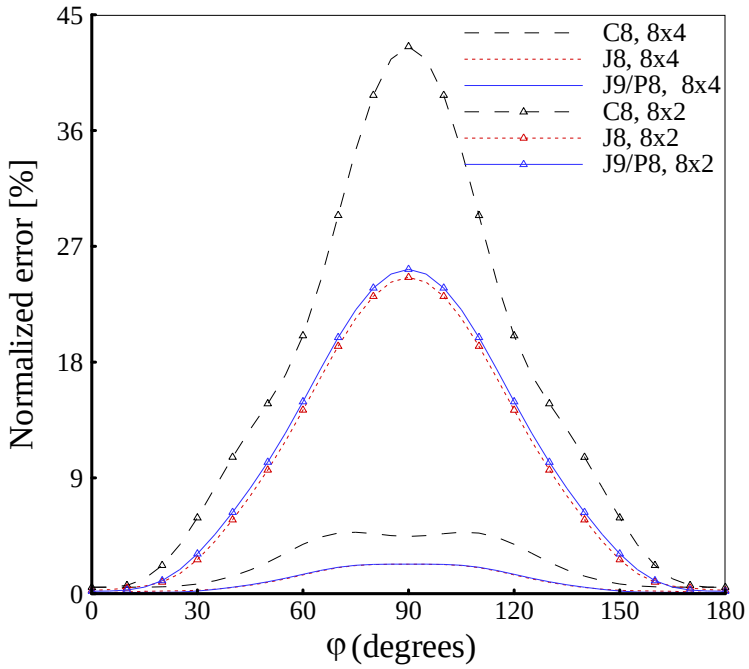

Figure 12. Normalized error of the eight-node elements at aspect ratio 2 (8×4 elements) and 4 (8×2 elements) with kL = 8, see Figure 4(b).

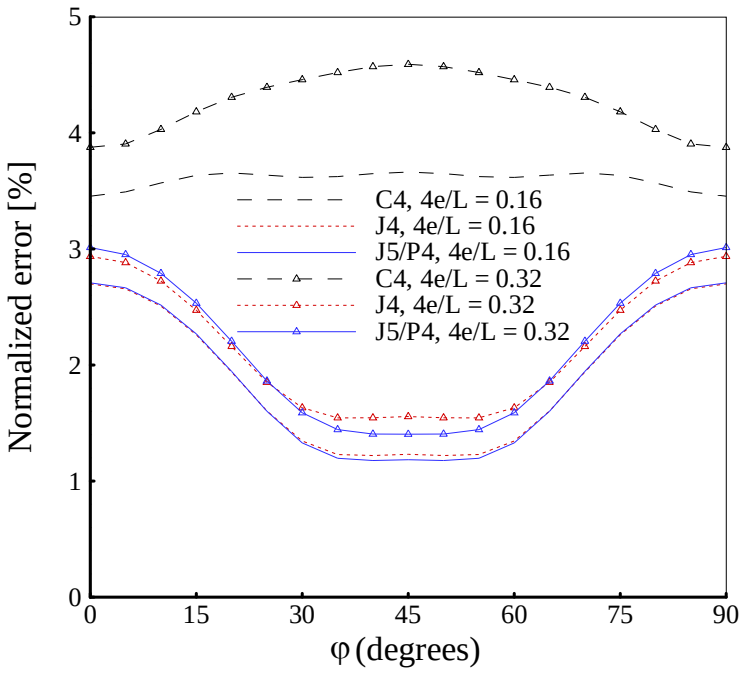

Figure 13. Normalized error of the four-node elements at different distortions "e". The problem domain is modeled by 16×16 elements with $k = 4$ and $L = 2$ ($N_n \approx 4\pi$), see Figure 4(b).

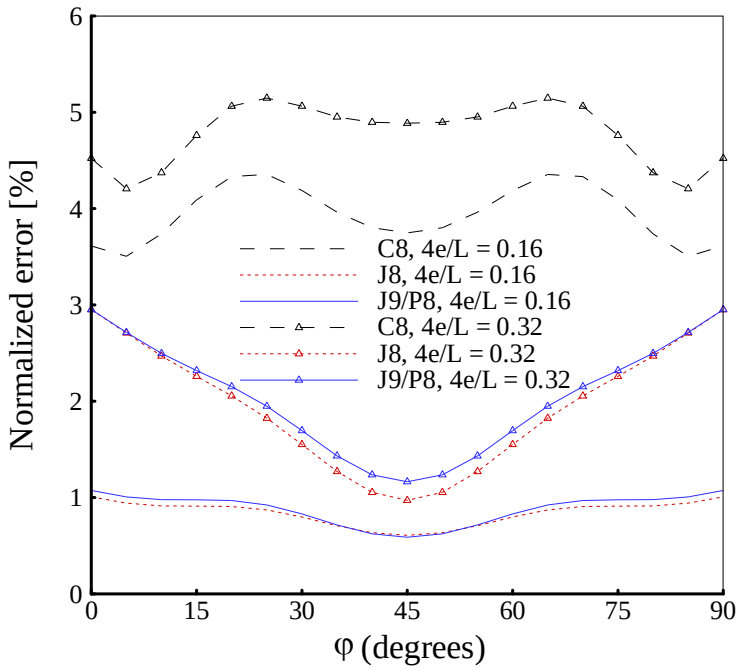

Figure 14. Normalized error of the eight-node elements at different distortions "e". The problem domain is modeled by 4×4 elements with $k = 4$ and $L = 2$ ($N_n \approx 2\pi$), see Figure 4(b).

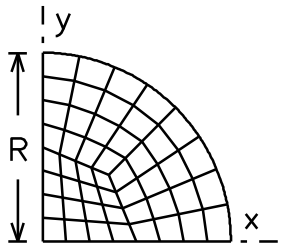

Figure 15. The quarter circular panel problem in which R equals unity. There are n (= 8) elements along each coordinate axis. The exact solution is $u = 2\,J_2(kr)\cos 2\theta / J_2(k)$.

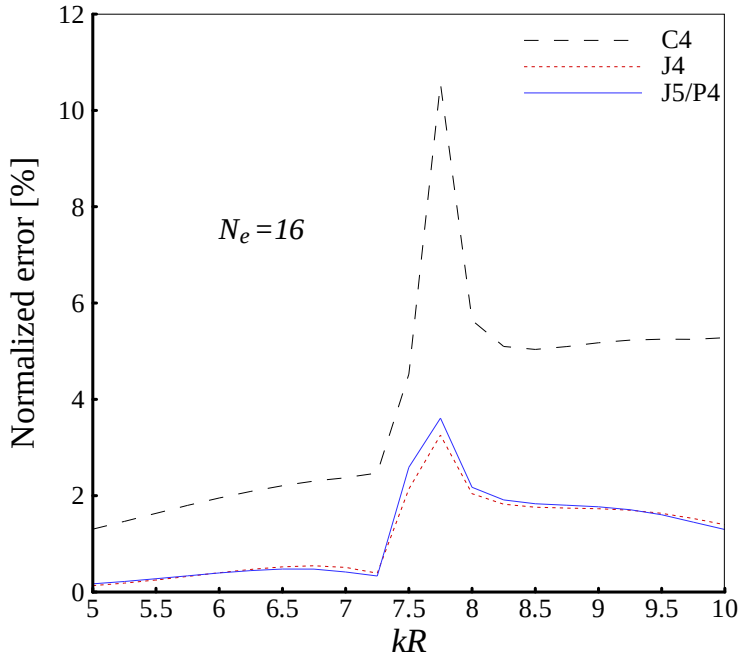

Figure 16. Normalized error of four-node elements for $5 < kR < 10$. There are 16 elements along each coordinate axis, see Figure 11. At kR = 5 and 10, N_n = 20.1 and 10.1, respectively, see Figure 15.

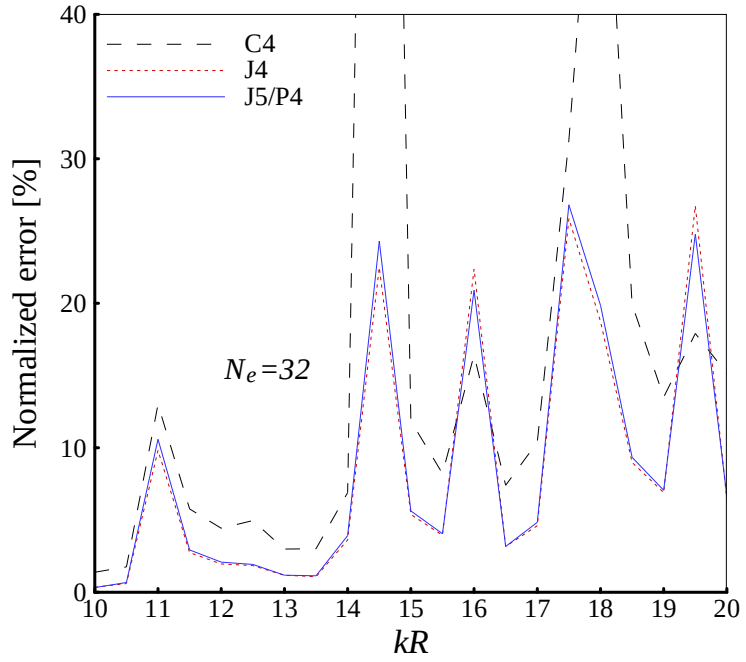

Figure 17. Normalized error of the four-node elements for $10 < kR < 20$ with 32 elements along each coordinate axis, see Figure 11. At kR = 10 and 20, N_n = 20.1 and 10.1, respectively, see Figure 15.

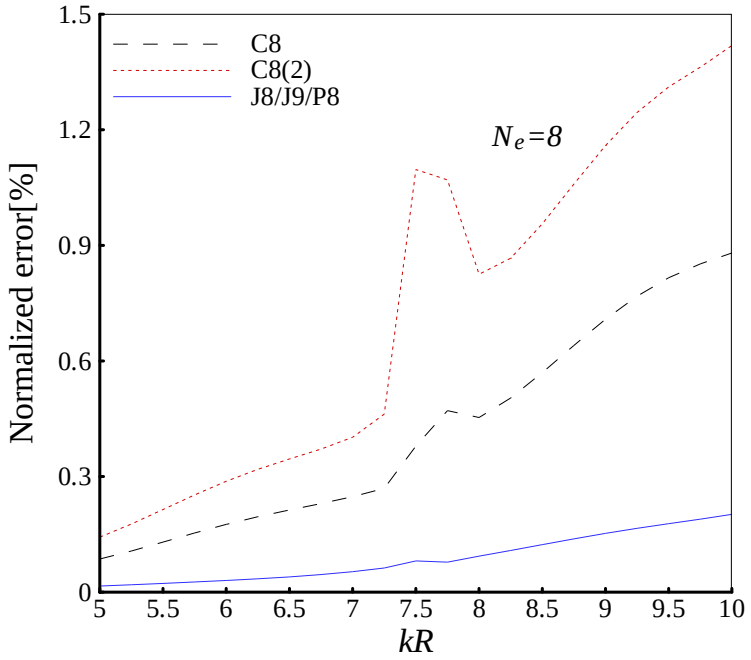

Figure 18. Normalized error of the eight-node elements for $5 < kR < 10$ with 8 elements along each coordinate axis, see Figure 11. At kR = 5 and 10, N_n = 20.1 and 10.1, respectively, see Figure 15.

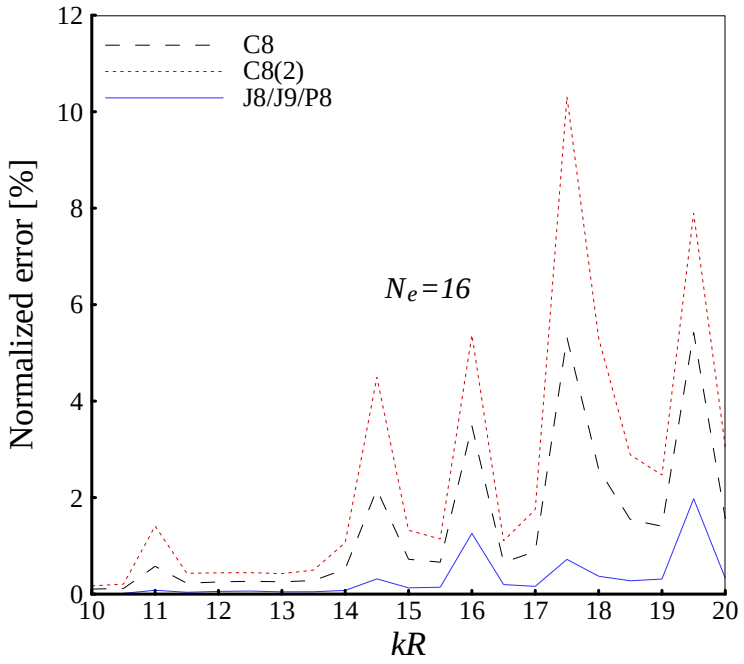

Figure 19. Normalized error of the eight-node elements for $10 < kR < 20$ with 16 elements along each coordinate axis, see Figure 11. At kR = 10 and 20, N_n = 20.1 and 10.1, respectively, see Figure 15.

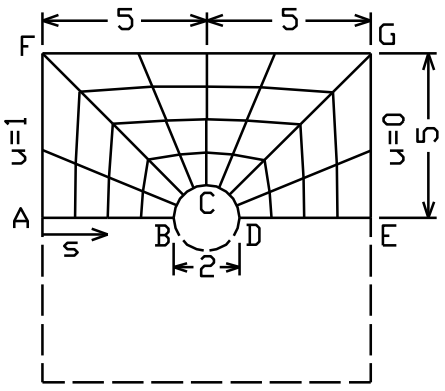

Figure 20. A square panel with a central circular obstacle. Owing to symmetry, only the upper half of the panel is modeled.

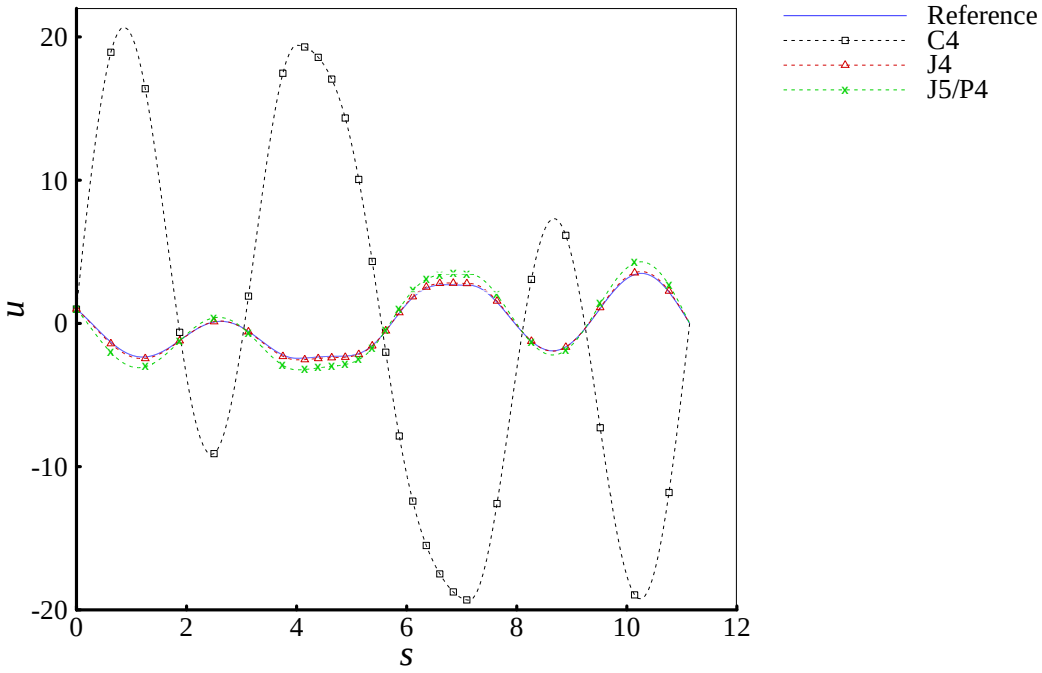

(a) Before zooming the ordinate.

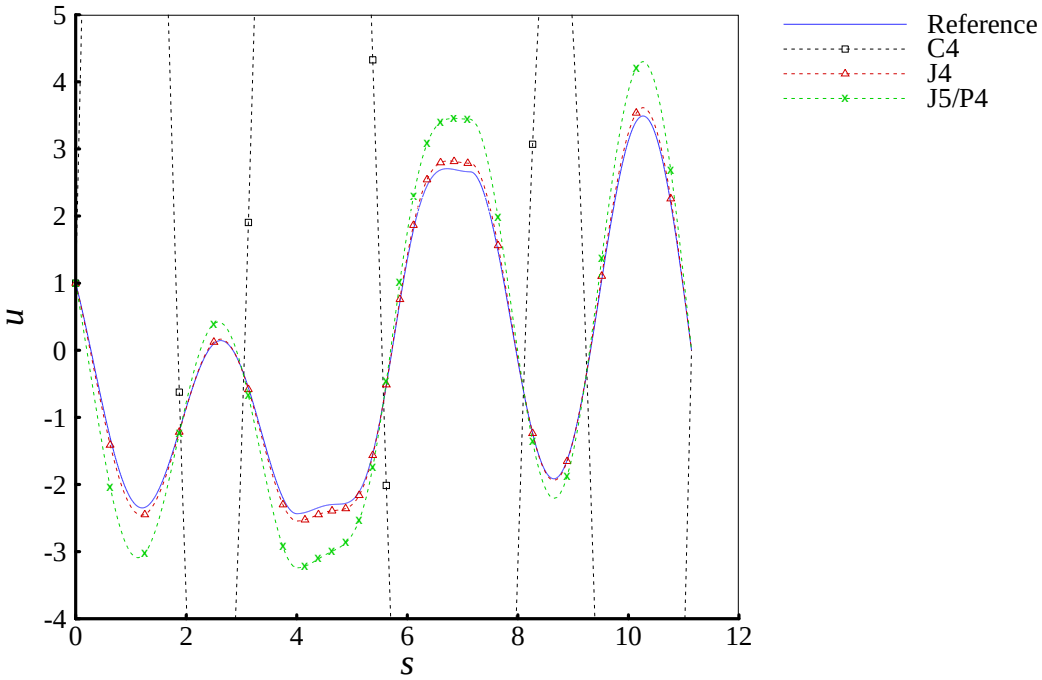

(b) After zooming the ordinate.

Figure 21. The nodal predictions (along ABCDE in Figure 16) obtained by 64×128 four-node elements for $k = 2$ and $N_n = 40.9$, see Figure 20.

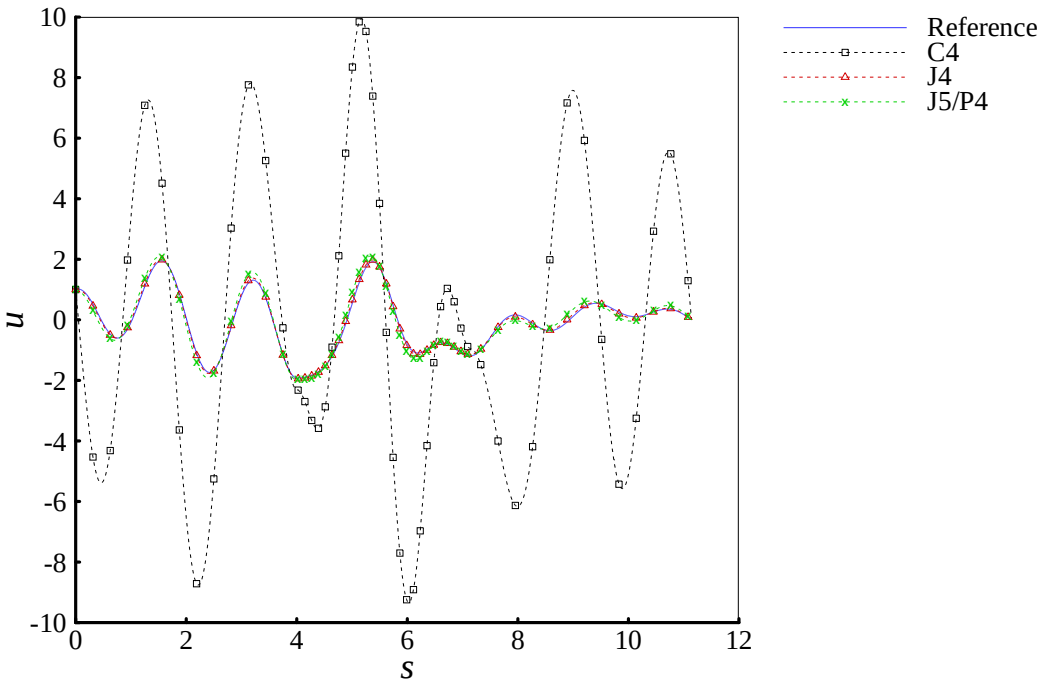

(a) Before zooming the ordinate.

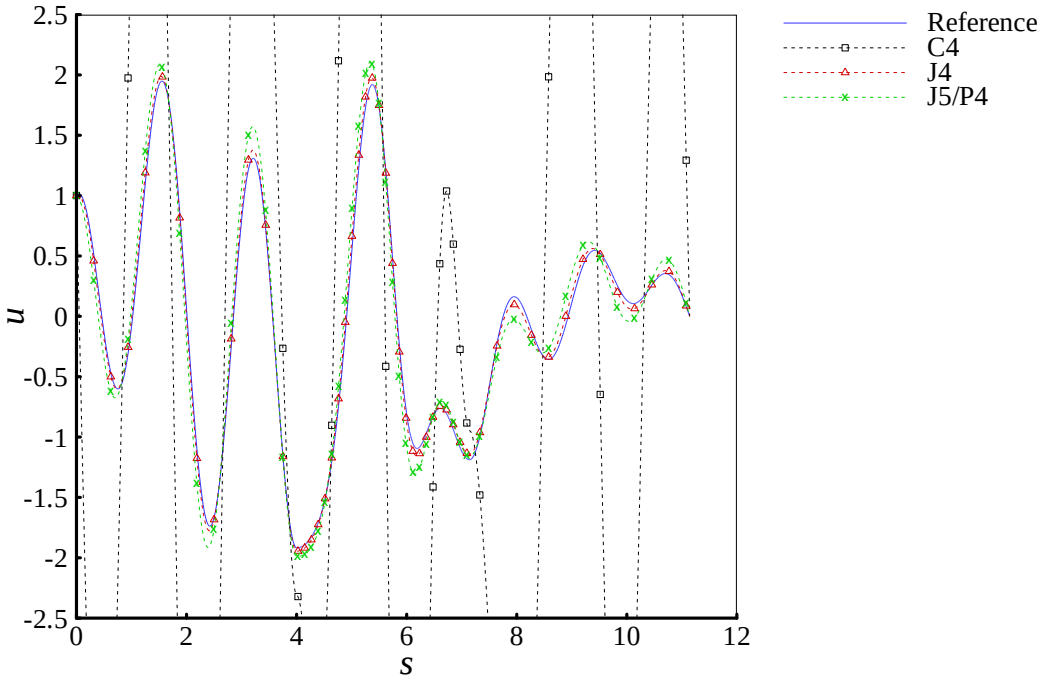

(b) After zooming the ordinate.

Figure 22. The nodal predictions (along ABCDE in Figure 16) obtained by 128×256 four-node elements for $k = 4$ and $N_n = 40.9$, see Figure 20.

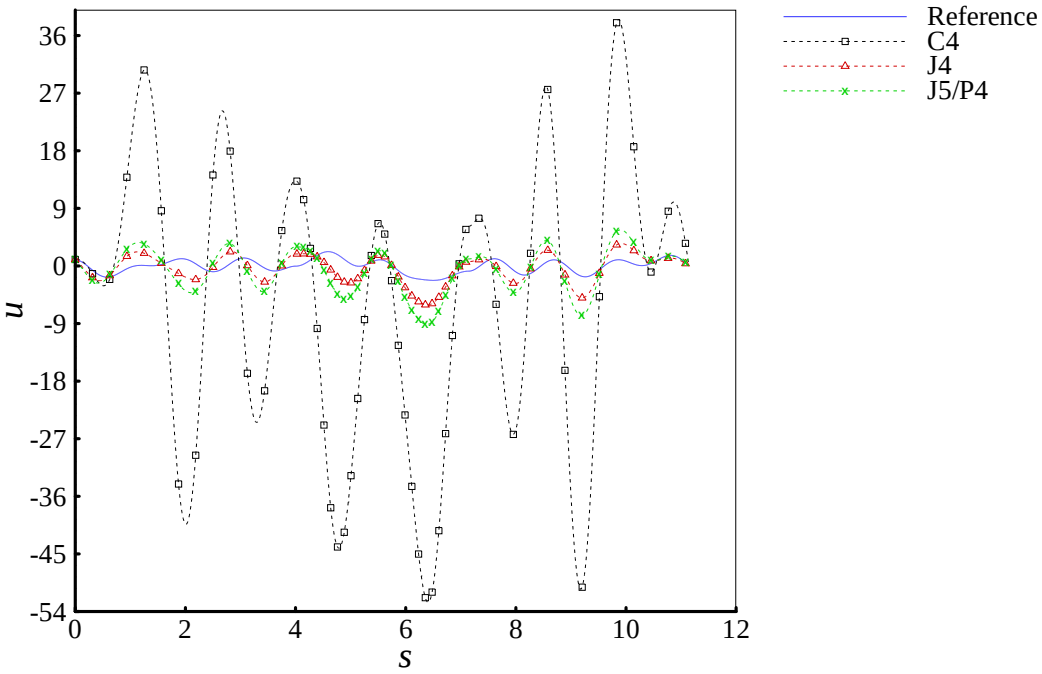

(a) Before zooming the ordinate.

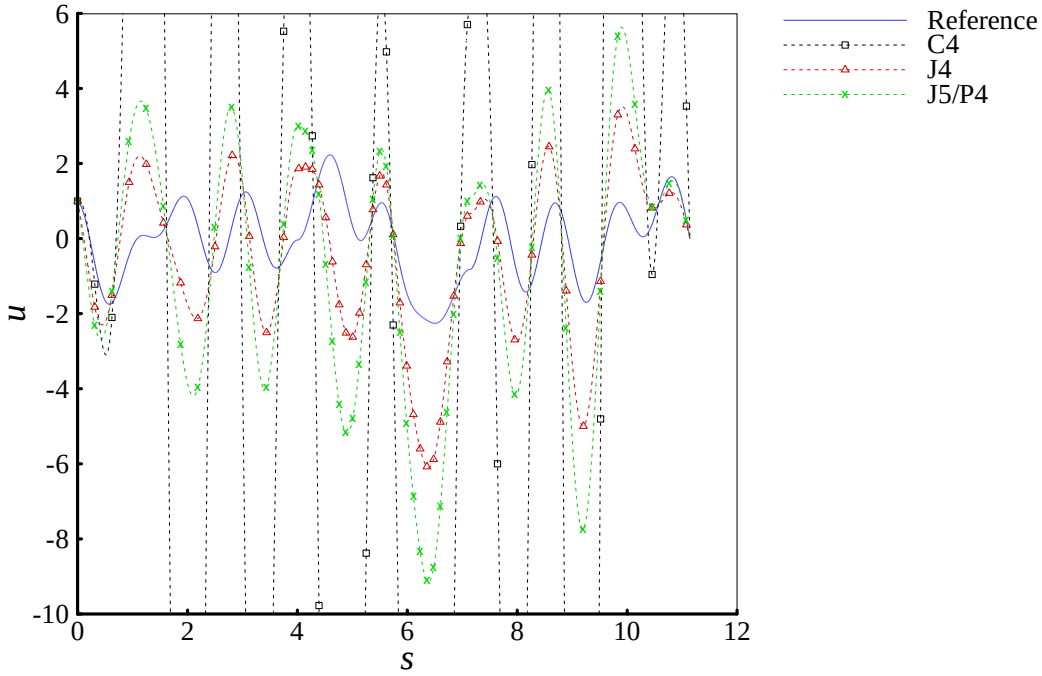

(b) After zooming the ordinate.

Figure 23. The nodal predictions (along ABCDE in Figure 16) obtained by 192×384 four-node elements for k = 6 and N_n = 40.9, see Figure 20.

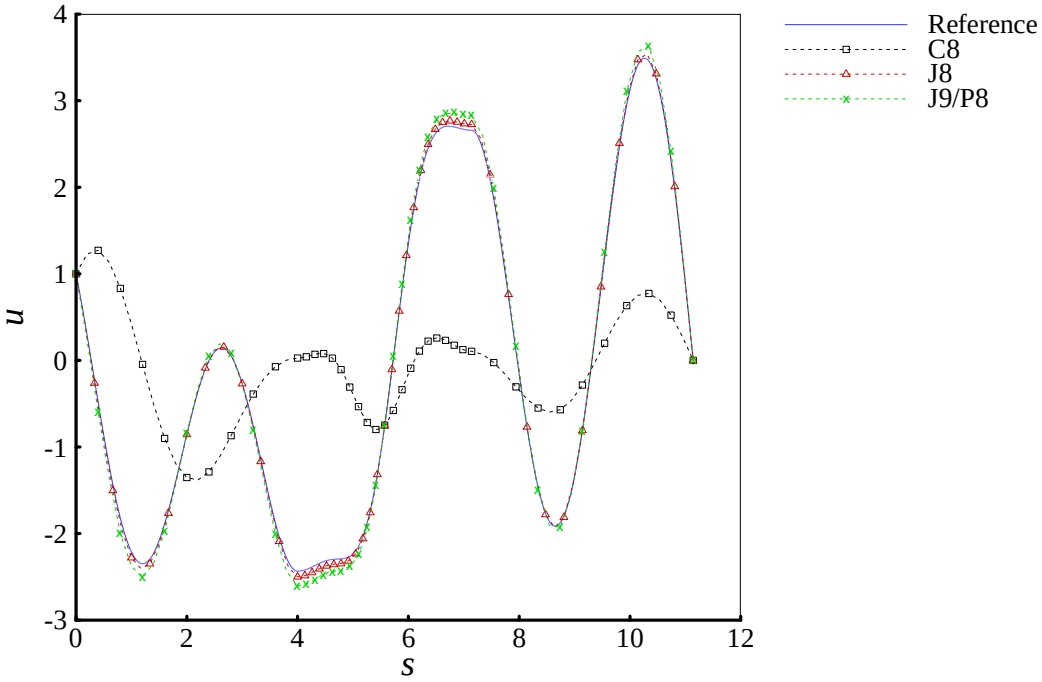

Figure 24. The nodal predictions (along ABCDE in Figure 16) obtained by 10×20 eight-node elements for $k = 2$ and $N_n = 12.8$, see Figure 20.

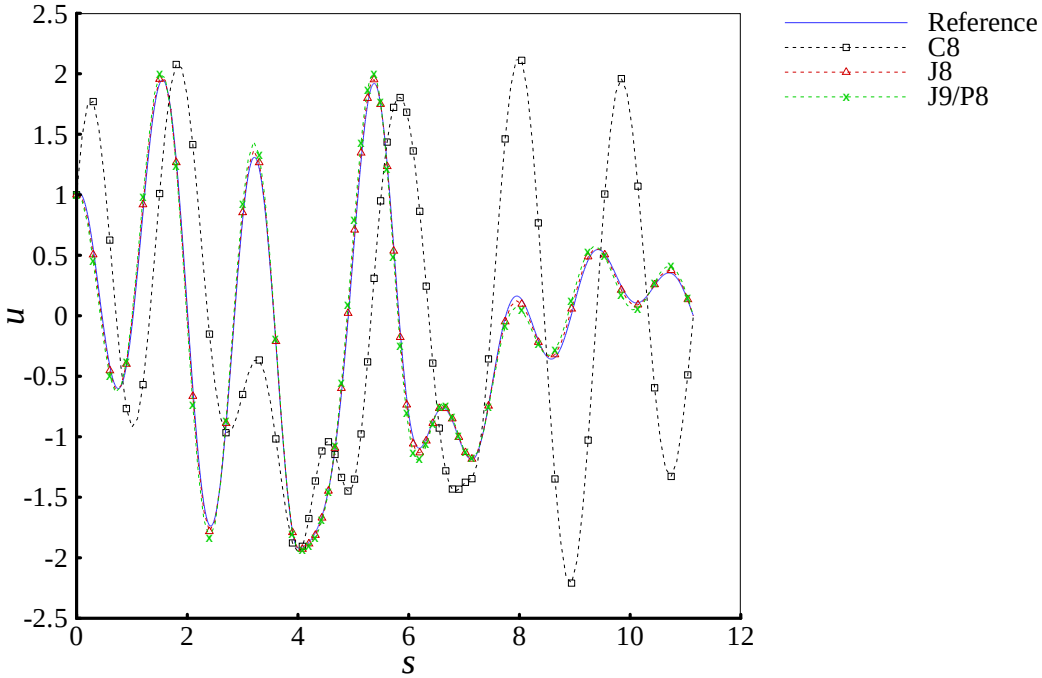

Figure 25. The nodal predictions (along ABCDE in Figure 16) obtained by 20×40 eight-node elements for $k = 4$ and $N_n = 12.8$, see Figure 20.

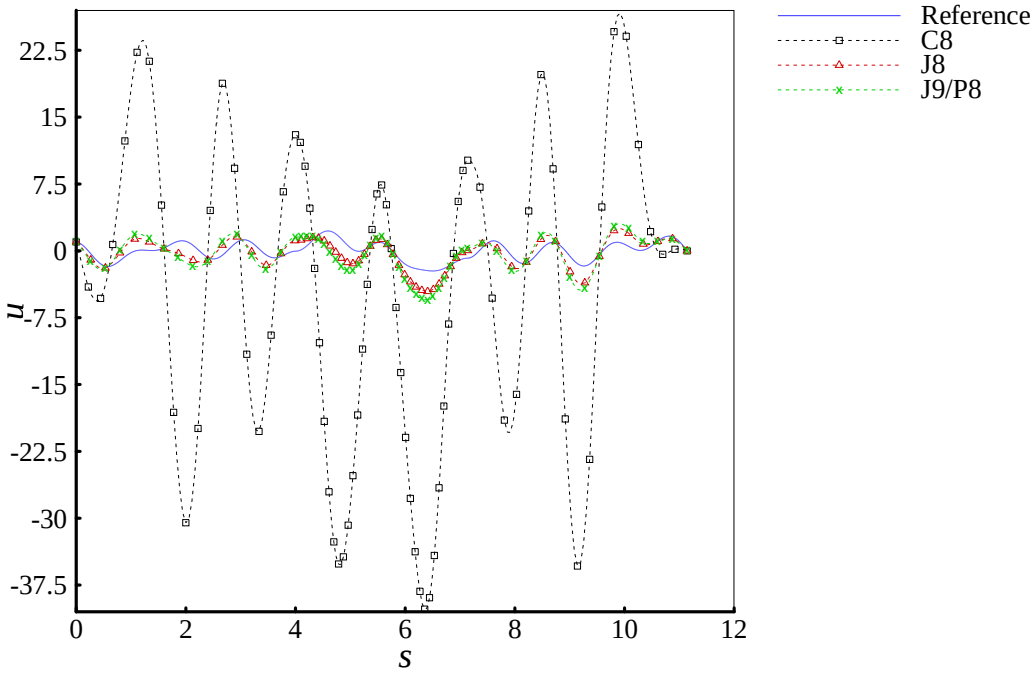

(a) Before zooming the ordinate.

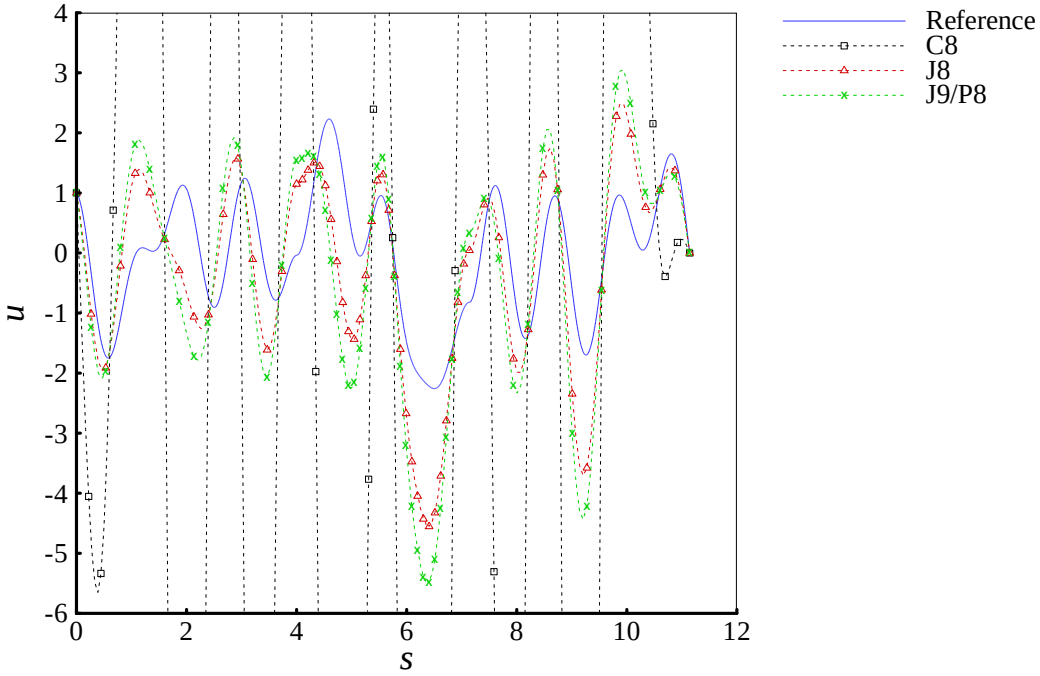

(b) After zooming the ordinate.

Figure 26. The nodal predictions (along ABCDE in Figure 16) obtained by 30×60 eight-node elements for k = 6 and N_n = 12.8, see Figure 20.

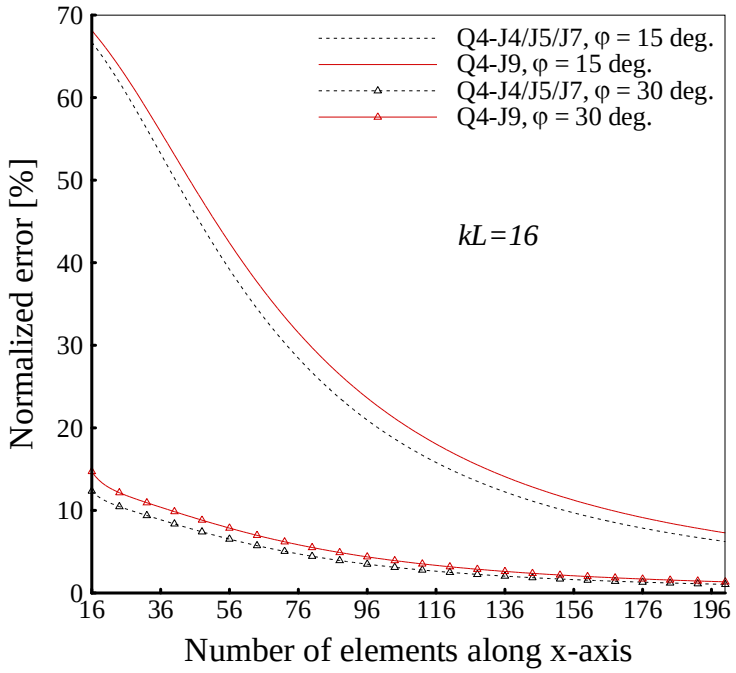

Figure 27. Convergence of hybrid four-node elements with different numbers of domain modes. When the number of element equals 16 and 196, N_n equals 2π and 24.5π, respectively, see Figure 4(a).

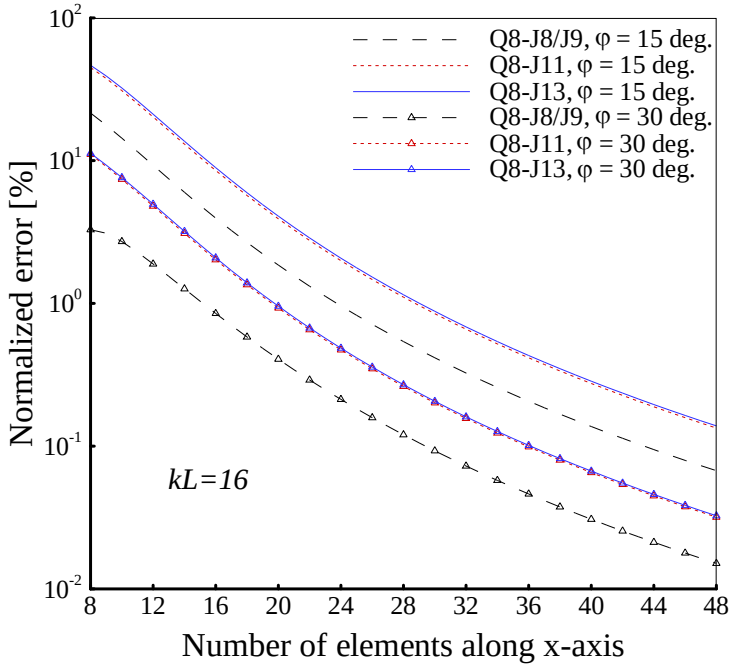

Figure 28. Convergence of hybrid eight-node elements with different numbers of domain modes. When the number of element equals 8 and 48, N_n equals 2π and 12π, respectively, see Figure 4(a).

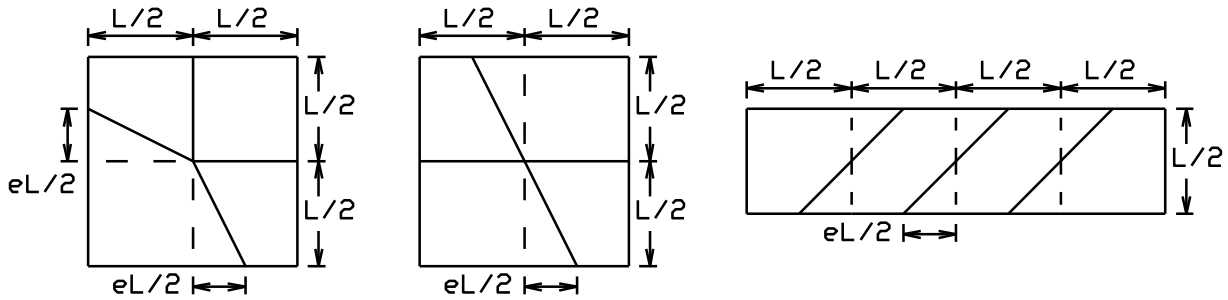

(a) (b) (c)

Figure 29. Meshes for studying the effect of element distortion in the plane wave problem with $k = 2$ and propagation angle $\varphi = \pi/8$. "e" is varied from 0 to 0.5. In (a) and (b), 8×8 nodal spacings are employed. In (c), 16×4 nodal spacings are employed. Hence, the average N_n is 4π.

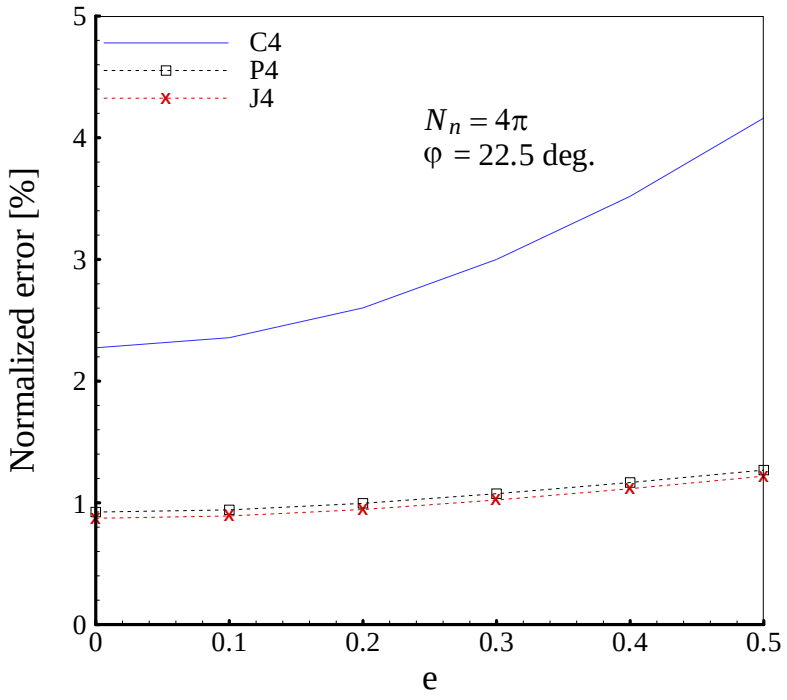

Figure 30. Normalized error of the four-node elements in the plane-wave problem using the mesh in Figure 29 (a) at different distortion "e".

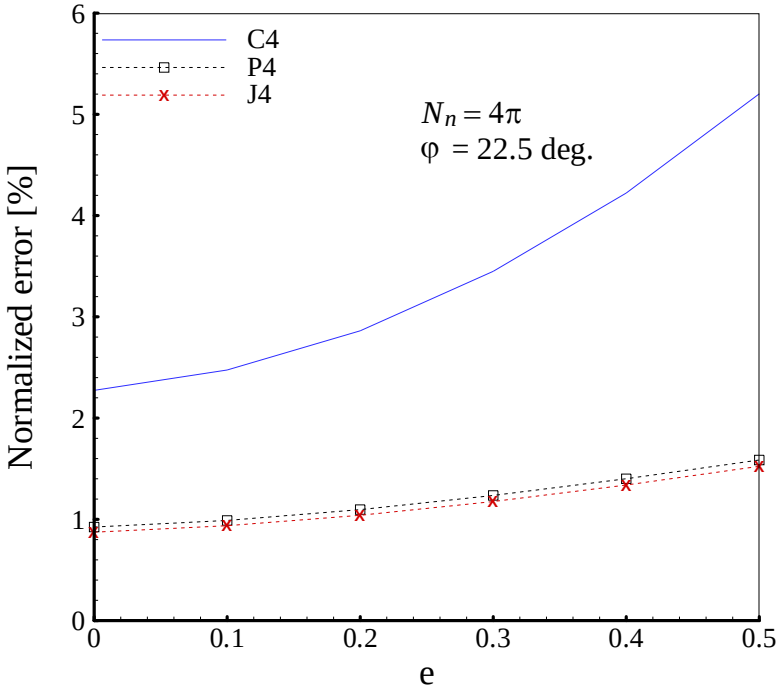

Figure 31. Normalized error of the four-node elements in the plane-wave problem using the mesh in Figure 29 (b) at different distortion "e".

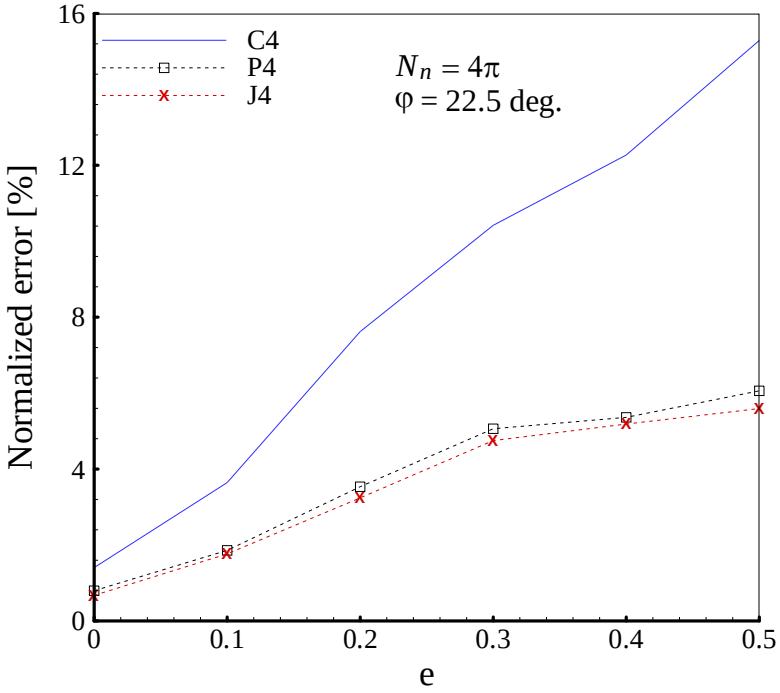

Figure 32. Normalized error of the four-node elements in the plane-wave problem using the mesh in Figure 29(c) at different distortion "e".

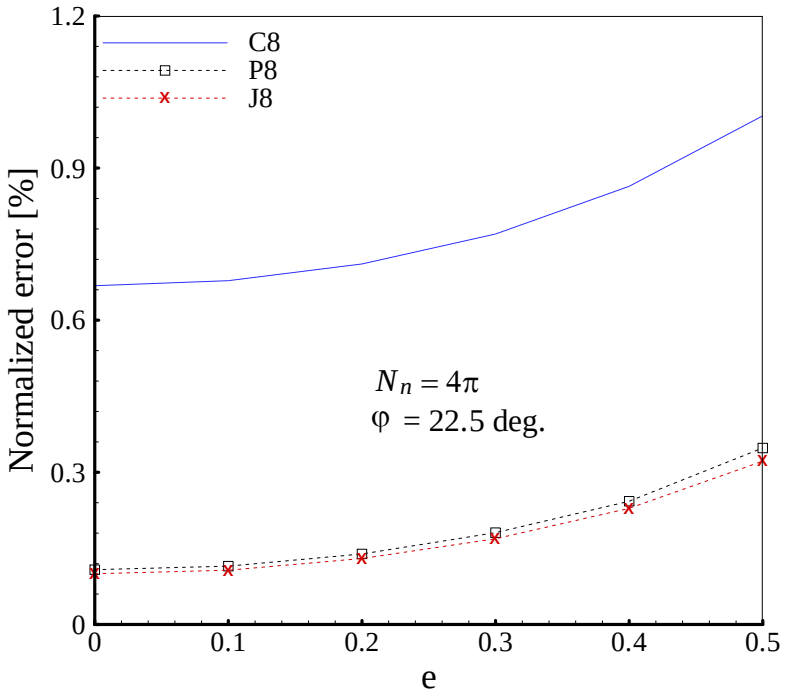

Figure 33. Normalized error of the eight-node elements in the plane-wave problem using the mesh in Figure 29 (a) at different distortion "e".

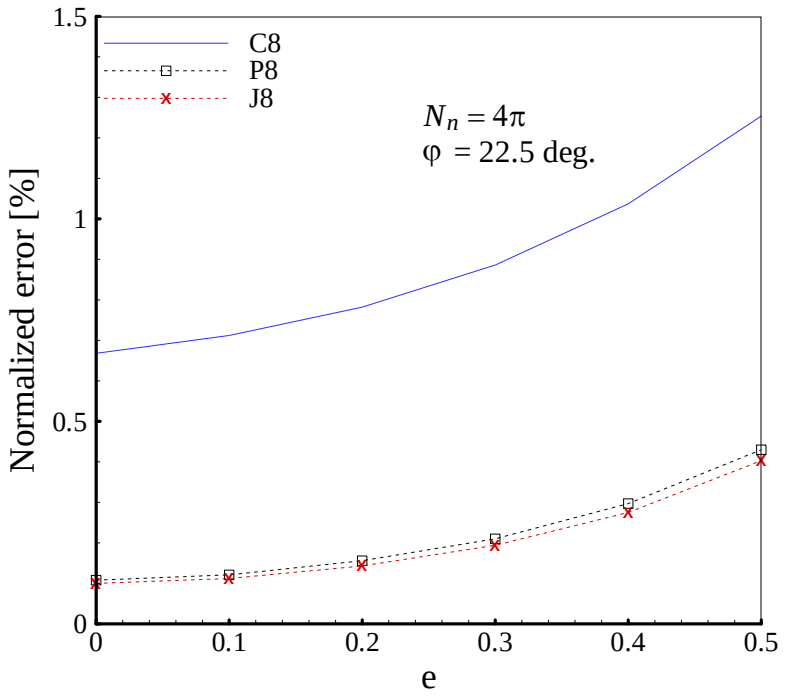

Figure 34. Normalized error of the eight-node elements in the plane-wave problem using the mesh in Figure 29 (b) at different distortion "e".

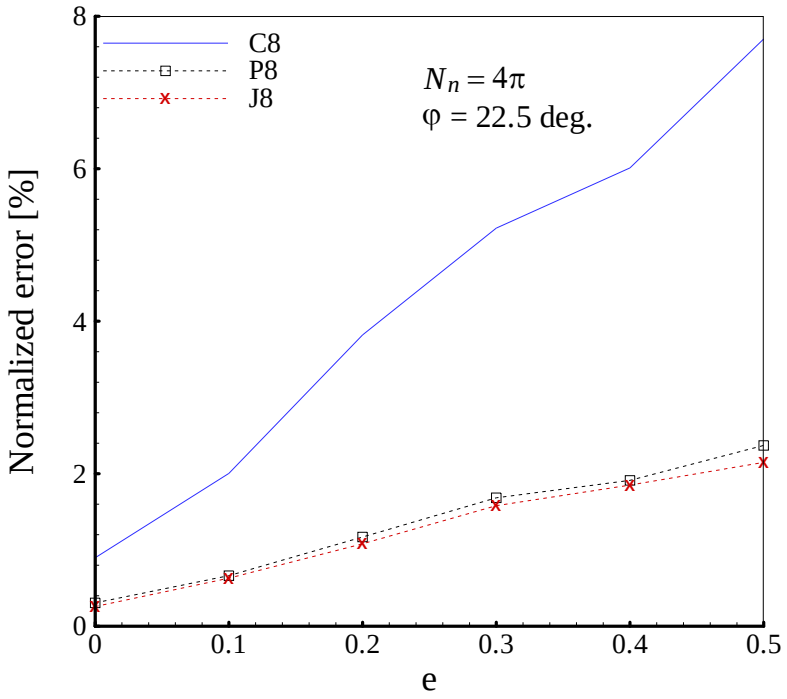

Figure 35. Normalized error of the eight-node elements in the plane-wave problem using the mesh in Figure 29(c) at different distortion "e".